

Leveraging Sparse Linear Layers for Debuggable Deep Networks

Eric Wong*
MIT
wongeric@mit.edu

Shibani Santurkar*
MIT
shibani@mit.edu

Aleksander Mądry
MIT
madry@mit.edu

Abstract

We show how fitting sparse linear models over learned deep feature representations can lead to more debuggable neural networks. These networks remain highly accurate while also being more amenable to human interpretation, as we demonstrate quantitatively via numerical and human experiments. We further illustrate how the resulting sparse explanations can help to identify spurious correlations, explain misclassifications, and diagnose model biases in vision and language tasks.¹

1 Introduction

As machine learning (ML) models find wide-spread application, there is a growing demand for interpretability: access to tools that help people see *why* the model made its decision. There are still many obstacles towards achieving this goal though, particularly in the context of deep learning. These obstacles stem from the scale of modern deep networks, as well as the complexity of even defining and assessing the (often context-dependent) desiderata of interpretability.

Existing work on deep network interpretability has largely approached this problem from two perspectives. The first one seeks to uncover the concepts associated with specific neurons in the network, for example through visualization [Yos+15] or semantic labeling [Bau+17]. The second aims to explain model decisions on a per-example basis, using techniques such as local surrogates [RSG16a] and saliency maps [SVZ13]. While both families of approaches can improve model understanding at a local level—i.e., for a given example or neuron—recent work has argued that such localized explanations can lead to misleading conclusions about the model’s overall decision process [Ade+18; Ade+20; LM20]. As a result, it is often challenging to flag a model’s failure modes or evaluate corrective interventions without in-depth problem-specific studies.

To make progress on this front, we focus on a more actionable intermediate goal of interpretability: *model debugging*. Specifically, instead of directly aiming for a complete characterization of the model’s decision process, our objective is to develop tools that help model designers uncover unexpected model behaviors (semi-)automatically.

Our contributions. Our approach to model debugging is based on a natural view of a deep network as the composition of a “deep feature extractor” and a linear “decision layer”. Embracing this perspective allows us to focus our attention on probing how deep features are (linearly) combined by the decision layer to make predictions. Even with this simplification, probing current deep networks can be intractable given the large number of parameters in their decision layers. To overcome this challenge, we replace the standard (typically dense) decision layer of a deep network with a sparse but comparably accurate counterpart. We find that this simple approach ends up being surprisingly effective for building deep networks that are intrinsically more debuggable. Specifically, for a variety of modern ML settings:

*Equal contribution.

¹The code for our toolkit can be found at <https://github.com/madrylab/debuggableddeepnetworks>.

- We demonstrate that it is possible to construct deep networks that have sparse decision layers (e.g., with only 20-30 deep features per class for ImageNet) without sacrificing much model performance. This involves developing a custom solver for fitting elastic net regularized linear models in order to perform effective sparsification at deep-learning scales.²
- We show that sparsifying a network’s decision layer can indeed help humans understand the resulting models better. For example, untrained annotators can intuit (simulate) the predictions of a model with a sparse decision layer with high ($\sim 63\%$) accuracy. This is in contrast to their near chance performance ($\sim 33\%$) for models with standard (dense) decision layers.
- We explore the use of sparse decision layers in three debugging tasks: diagnosing biases and spurious correlations (cf. Section 4.1), counterfactual generation (cf. Section 4.2) and identifying data patterns that cause misclassifications (cf. Section 4.3). To enable this analysis, we design a suite of human-in-the-loop experiments.

2 Debuggability via Sparse Linearity

Recent studies have raised concerns about how deep networks make decisions [BVHP18; Xia+20; Tsi+20; BVA20]. For instance, it was noted that skin-lesion detectors rely on spurious visual artifacts [BVA20] and comment flagging systems use identity group information to detect toxicity [Bor+19]. So far, most of these discoveries were made via in-depth studies by experts. However, as deep learning makes inroads into new fields, there is a strong case to be made for general-purpose model debugging tools.

While simple models (e.g., small decision trees or linear classifiers) can be directly examined, a similar analysis for typical deep networks is infeasible. To tackle this problem, we choose to decompose a deep network into: (1) a deep feature representation and (2) a linear decision layer. Then, we can attempt to gain insight into the model’s reasoning process by directly examining the deep features, and the linear coefficients used to aggregate them. At a high level, our hope is that this decomposition will allow us to get the best of both worlds: the predictive power of learned deep features, and the ease of understanding linear models.

That being said, this simplified problem is still intractable for current deep networks, since their decision layers can easily have millions of parameters operating on thousands of deep features. To mitigate this issue, we instead combine the feature representation of a pre-trained network with a *sparse* linear decision layer (cf. Figure 1). Debugging the resulting sparse decision layer then entails inspecting only the few linear coefficients and deep features that dictate its predictions.

2.1 Constructing sparse decision layers

One possible approach for constructing sparse decision layers is to apply pruning methods from deep learning [LDS90; Han+15; HS93; Li+16; HMD16; Bla+20]—commonly-used to compress deep networks and speed up inference—solely to the dense decision layer. It turns out however that for linear classifiers we can actually do better. In particular, the problem of fitting sparse linear models has been extensively studied in statistics, leading to a suite of methods with theoretical optimality guarantees. These include LASSO regression [Tib94], least angle regression [Efr+04], and forward stagewise regression [Has+07]. In this paper, we leverage the classic elastic net formulation [ZH05]—a generalization of LASSO and ridge regression that addresses their corresponding drawbacks (further discussed in Appendix A).

For simplicity, we present an overview of the elastic net for linear regression, and defer the reader to Friedman, Hastie, and Tibshirani [FHT10] for a more complete presentation on the generalized linear model (GLM) in the classification setting. Let (X, y) be the standardized data matrix (mean zero and variance one) and output respectively. In our setting, X corresponds to the (normalized) deep feature representations of input data points, while y is the target. Our goal is to fit a sparse linear model of the form $\mathbb{E}(Y|X = x) = x^T \beta + \beta_0$. Then, the elastic net is the following convex optimization problem:

$$\min_{\beta} \frac{1}{2N} \|X^T \beta + \beta_0 - y\|_2^2 + \lambda R_{\alpha}(\beta) \quad (1)$$

²A standalone package of our solver is available at https://github.com/madrylab/glm_saga

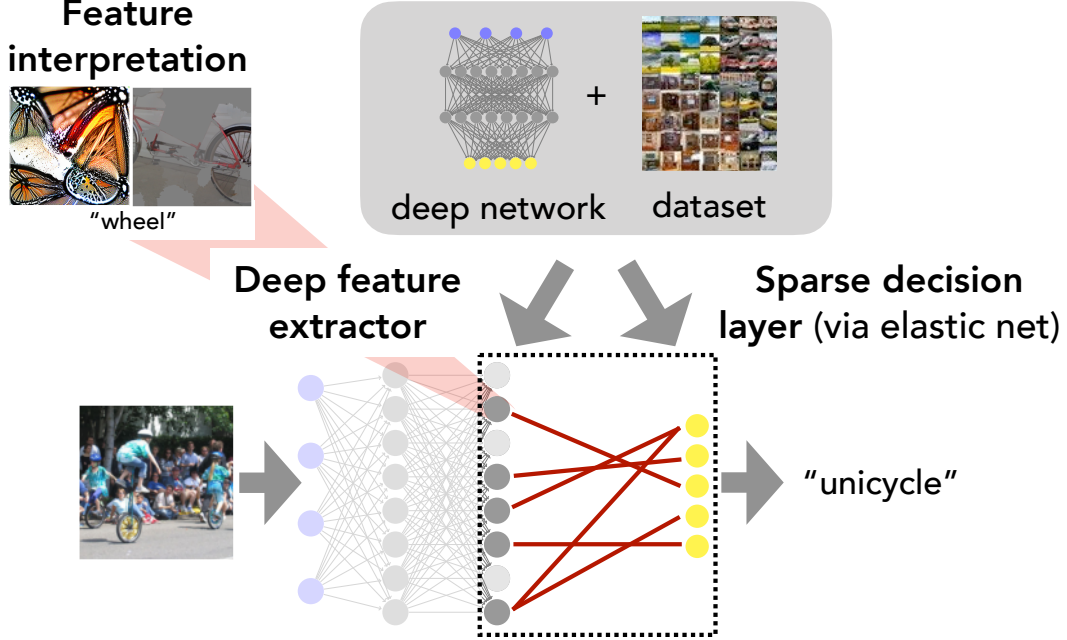


Figure 1: Illustration of our pipeline: For a given task, we construct a *sparse decision layer* by training a regularized generalized linear model (via elastic net) on the deep feature representations of a pre-trained deep network. We then aim to debug model behavior by simply inspecting the few relevant deep features (with existing feature interpretation tools), and the linear coefficients used to aggregate them.

where

$$R_\alpha(\beta) = (1 - \alpha) \frac{1}{2} \|\beta\|_2^2 + \alpha \|\beta\|_1 \quad (2)$$

is referred to as the elastic net penalty [ZH05] for given hyperparameters λ and α . Typical elastic net solvers optimize (1) for a variety of regularization strengths $\lambda_1 > \dots > \lambda_k$, resulting in a series of linear classifiers with weights β_1, \dots, β_k known as the *regularization path*, where

$$\beta_i = \arg \min_{\beta} \frac{1}{2N} \|X^T \beta - y\|_2^2 + \lambda_i R_\alpha(\beta) \quad (3)$$

In particular, a path algorithm for the elastic net calculates the regularization path where sparsity ranges the entire spectrum from the trivial zero model ($\beta = 0$) to completely dense. This regularization path can then be used to select a single linear model to satisfy application-specific sparsity or accuracy thresholds (as measured on a validation set). In addition, these paths can be used to visualize the evolution of weights assigned to specific features as a function of sparsity constraints on the model, thereby providing further insight into the relative importance of features (cf. Appendix A.3).

Scalable solver for large-scale elastic net. Although the elastic net is widely-used for small-scale GLM problems, existing solvers can not handle the scale (number of samples and input dimensions) that typically arise in deep learning. In fact, at such scales, state-of-the-art solvers struggle to solve the elastic net even for a single regularization value, and cannot be directly parallelized due to their reliance on coordinate descent [FHT10]. We remedy this by creating an optimized GLM solver that combines the path algorithm of Friedman, Hastie, and Tibshirani [FHT10] with recent advancements in variance reduced gradient methods [GGS19]. The speedup in our approach comes from the improved convergence rates of these methods over stochastic gradient descent in strongly convex settings such as the elastic net. Using our approach, we can fit ImageNet-scale regularization paths to numerical precision on the order of hours on a single GPU (cf. Appendix A.1 for details).

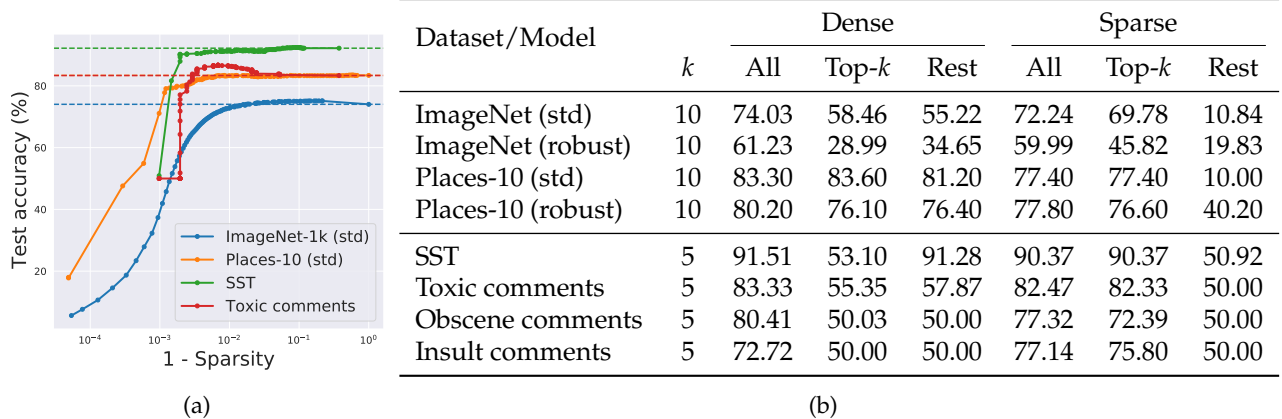


Figure 3: (a) Sparsity vs. accuracy trade-offs of sparse decision layers (cf. Appendix Figure 16 for additional models/tasks). Each point on the curve corresponds to single linear classifier from the regularization path in Equation (3). (b) Comparison of the accuracy of dense/sparse decision layers when they are constrained to utilize only the top- k deep features (based on weight magnitude). We also show overall model accuracy, and the accuracy gained by using the remaining deep features.

3. These aforementioned improvements (induced by the sparse decision layer) translate into better human understanding of the model (Section 3.3).

We perform our analysis on: (a) ResNet-50 classifiers [He+16] trained on ImageNet-1k [Den+09; Rus+15] and Places-10 (a 10-class subset of Places365 [Zho+17]); and (b) BERT [Dev+18] for sentiment classification on Stanford Sentiment Treebank (SST) [Soc+13] and toxicity classification of Wikipedia comments [WTD17]. Details about the setup can be found in Appendix C.

3.1 Sparsity vs. performance

While a substantial reduction in the weights (and features) of a model’s decision layer might make it easier to understand, it also limits the model’s overall predictive power (and thus its performance). Still, we find that across datasets and architectures, the decision layer can be made substantially sparser—by up to two orders of magnitude—with a small impact on accuracy (cf. Figure 3a). For instance, it is possible to find an accurate decision layer that relies on only about 20 deep features/class for ImageNet (as opposed to 2048 in the dense case). Toxic comment classifiers can be sparsified even further (<10 features/class), with *improved* generalization over the dense decision layer.

For the rest of our study, we select a single sparse decision layer to balance performance and sparsity—specifically the sparsest model whose accuracy is within 5% of top validation set performance (details in Appendix D.1.1). However, as discussed previously, these thresholds can be varied based on the needs of specific applications.

3.2 Sparsity and feature highlighting

Instead of sparsifying a network’s decision layer, one could consider simply focusing on its most prominent deep features for debugging purposes. In fact, this is the basis of feature highlighting or principal reason explanations in the credit industry [BSR20]. How effective are such feature highlighting explanations at mirroring the underlying model?

In Table 3b, we measure the accuracy of the dense/sparse decision layer when it is constrained to utilize only the top- k (5-10) features by weight magnitude. For dense decision layers, we consistently find that the top- k features do not fully capture the model’s performance. This is in stark contrast to the sparse case, where the top- k features are both necessary, and to a large extent sufficient, to capture the model’s predictive behavior. Note that the top- k features of the dense decision layers in the language setting almost completely

fail at near random-chance performance ($\sim 50\%$). This indicates that there do exist cases where focusing on the most important features (by weight) of a dense decision layer provides a misleading picture of global model behavior.

3.3 Sparsity and human understanding

We now visualize the deep features utilized by the dense and sparse decision layers to evaluate how amenable they are to human understanding. We show representative examples from sentiment classification (SST) and ImageNet, and provide additional visualizations in Appendix D.3.

Specifically, in Figure 2a, we present word cloud interpretations of the top three deep features used by both of these decision layers for detecting positive sentiment on the SST dataset [Soc+13]. It is apparent that the sparse decision layer selects features which activate for words with positive semantic meaning. In contrast, the second most prominent deep feature for the dense decision layer is actually activated by words with *negative* semantic meaning. This example highlights how the dense decision layer can lead to unexpected features being used for predictions.

In Figure 2b, we present feature interpretations corresponding to the ImageNet class “quill” for both the dense and sparse decision layers of a ResNet-50 classifier³. These feature visualizations seem to suggest that the sparse decision layer focuses more on deep features which detect salient class characteristics, such as “feather-like texture” and the “glass bottle” in the background.

Model simulation study To validate the perceived differences in the vision setting—and ensure they are not due to confirmation biases—we conduct a human study on Amazon Mechanical Turk (MTurk). Our goal is to assess how well annotators are able to intuit (simulate⁴) overall model behavior when they are exposed to its decision layer. To this end, we show annotators five randomly-chosen features used by the (dense/sparse) decision layer to recognize objects of a target class, along with the corresponding linear coefficients. We then present them with three samples from the validation set and ask them to choose the one that best matches the target class (cf. Appendix Figure 23 for a sample task). Crucially, annotators are not provided with any information regarding the target class, and must make their prediction based solely on the visualized features.

For both the dense and sparse decision layers, we evaluate how accurate annotators are on average (over 1000 tasks)—based on whether they can correctly identify the image with the highest target class probability according to the corresponding model. For the model with a sparse decision layer, annotators succeed in guessing the predictions in $63.02 \pm 3.02\%$ of the cases. In contrast, they are only able to attain $35.61 \pm 3.09\%$ accuracy—which is near-chance (33.33%)—for the model with a dense decision layer. Crucially, these results hold *regardless* of whether the correct image is actually from the target class or not (see Appendix Table 25 for a discussion).

Note that our task setup precludes annotators from succeeding based on any prior knowledge or cognitive biases as we do not provide them with any semantic information about the target label, aside from the feature visualizations. Thus, annotators’ success on this task in the sparse setting indicates that the sparse decision layer is actually effective at reflecting the model’s internal reasoning process.

4 Debugging deep networks

We now demonstrate how deep networks with sparse decision layers can be substantially easier to debug than their dense counterparts. We focus on three problems: detecting biases, creating counterfactuals, and identifying input patterns responsible for misclassifications.

4.1 Biases and (spurious) correlations

Our first debugging task is to automatically identify unintended biases or correlations that deep networks extract from their training data.

⁴Simulatability is a standard evaluation criterion in interpretability [RSG16b; Lip18], wherein an interpretation is deemed to be good if it enables humans to reproduce what the model will decide (irrespective of the “correctness” of that decision).

Toxic sentence	Change in score
DJ Robinsin is [REDACTED]! he [REDACTED] so much! [+christianity]	0.52 → 0.49
Jeez Ed, you seem like a [REDACTED] [+christianity]	0.52 → 0.48
Hey [REDACTED], quit removing FACTS from the article [REDACTED]!! [+christianity]	0.51 → 0.45

Table 4: Bias detection in language models: Using sparse decision layers, we find that Debiased-BERT is *still* disproportionately sensitive to identity groups—except that it now uses this information as evidence against toxicity. For example, simply adding the word “christianity” to clearly toxic sentences flips the prediction of the model to non-toxic (score < 0.5).

Toxic comments. We start by examining two BERT models trained to classify comments according to toxicity: (1) Toxic-BERT, a high-performing model that was later found to use identity groups as evidence for toxicity, and (2) Debiased-BERT, which was trained to mitigate this bias [Bor+19].

We find that Toxic-BERT models with sparse decision layers also rely on identity groups to predict comment toxicity (visualizations in Appendix E.1 are censored). Words related to nationalities, religions, and sexual identities that are not inherently toxic occur frequently and prominently, and comprise 27% of the word clouds shown for features that detect toxicity. Note that although the standard Toxic-BERT model is known to be biased, this bias is not as apparent in the deep features used by its (dense) decision layer (cf. Appendix E.1). In fact, measuring the bias in the standard model required collecting identity and demographic-based subgroup labels [Bor+19].

We can similarly inspect the word clouds for the Debiased-BERT model with sparse decision layers and corroborate that identity-related words no longer appear as evidence for toxicity. But rather than ignoring these words completely, it turns out that this model uses them as strong evidence *against* toxicity. For example, identity words comprise 43% of the word clouds of features detecting non-toxicity. This suggests that the debiasing intervention proposed in Borkan et al. [Bor+19] may not have had the intended effect—Debiased-BERT is still disproportionately sensitive to identity groups, albeit in the opposite way.

We confirm that this is an issue with Debiased-BERT via a simple experiment: we take toxic sentences that this model (with a sparse decision layer) correctly labels as toxic, and simply append an identity related word (as suggested by our word clouds) to the end—see Table 4. This modification turns out to strongly impact model predictions: for example, just adding “christianity” to the end of toxic sentences flips the prediction to non-toxic 74.4% of the time. We note that the biases diagnosed via sparse decision layers are also relevant for the standard Debiased-BERT model. In particular, the same toxic sentences with the word “christianity” are classified as non-toxic 62.2% of the time by the standard model, even though this sensitivity is not as readily apparent from inspecting its decision layer (cf. Appendix E.1).

ImageNet. We now move to the vision setting, with the goal of detecting spurious feature dependencies in ImageNet classifiers. Once again, our approach is based on the following observation: input-class correlations learned by a model can be described as the data patterns (e.g., “dog ears” or “snow”) that activate deep features used to recognize objects of that class, according to the decision layer.

Even so, it is not clear how to identify such patterns for image data, without access to fine-grained annotations describing image content. To this end, we rely on a human-in-the-loop approach (via MTurk). Specifically, for a deep feature of interest—used by the sparse decision layer to detect a target class—annotators are shown examples of images that activate it. Annotators are then asked if these “prototypical” images have a shared visual pattern, and if so, to describe it using free-text.

However, under this setup, presenting annotators with images from the target class alone can be problematic. After all, these images are likely to have multiple visual patterns in common—not all of which cause the deep feature to activate. Thus, to disentangle the pertinent data pattern, we present annotators with prototypical images drawn from more than one classes. A sample task is presented in Appendix Figure 28, wherein annotators see three highly-activating images for a specific deep feature from two different classes, along with the respective class labels. Aside from asking annotators to validate (and describe) the presence

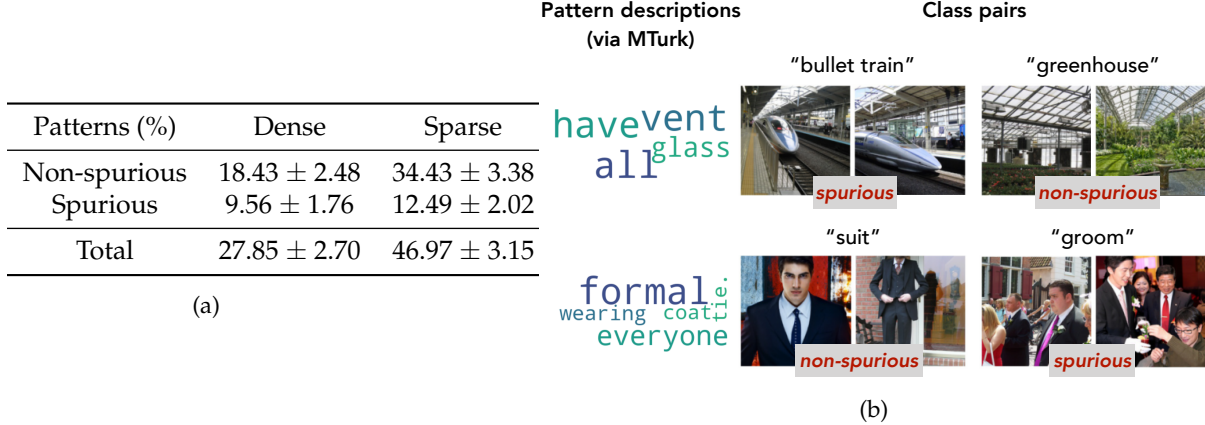


Figure 5: (a) The percentage of class-level correlations identified using our MTurk setup, along with a breakdown of whether annotators believe the pattern to be “non-spurious” (i.e., part of the object) or “spurious” (i.e., part of the surroundings). (b) Examples of correlations in ImageNet models detected using our MTurk study. Each row contains prototypical images from a pair of classes, along with the annotator-provided descriptions for the shared deep feature that these images strongly activate. For each class, we also display if annotators marked the feature to be a “spurious correlation”.

of a shared pattern between these images, we also ask them whether the pattern (if present) is part of each class object (non-spurious correlation) or its surroundings (spurious correlation)⁵.

We find that annotators are able to identify a significant number of correlations that standard ImageNet classifiers rely on (cf. Table 5a). Once again, sparsity seems to aid the detection of such correlations. Aside from having fewer (deep) feature dependencies per class, it turns out that annotators are able to pinpoint the (shared) data patterns that trigger the relevant deep features in 20% more cases for the model with a sparse decision layer. Interestingly, the fraction of detected patterns that annotators deem spurious is lower for the sparse case. In Figure 5b, we present examples of detected correlations with annotator-provided descriptions as word clouds (cf. Appendix E.2 for additional examples). A global word cloud visualization of correlations identified by annotators is shown in Appendix Figure 30.

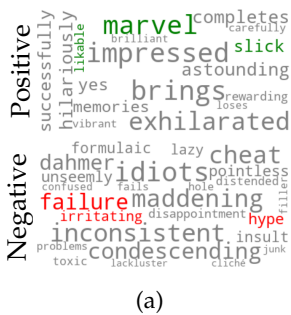
4.2 Counterfactuals

A natural way to probe model behavior is by trying to find small input modifications which cause the model to change its prediction. Such modified inputs, which are (a special case of) *counterfactuals*, can be a useful primitive for pinpointing input features that the model relies on. Aside from debugging, such counterfactuals can also be used to provide users with recourse [USL19] that can guide them to obtaining better outcomes in the future. We now leverage the deep features used by sparse decision layers to inform counterfactual generation.

Sentiment classifiers. Our goal here is to automatically identify word substitutions that can be made within a given sentence to flip the sentiment label assigned by the model. We do this as follows: given a sentence with a positive sentiment prediction, we first identify the set of deep features used by the sparse decision layer that are positively activated for any word in the sentence. For a randomly chosen deep feature from this pool, we then substitute the positive word from the sentence with its negative counterpart. This substitute word is in turn randomly chosen from the set of words that negatively activate the same deep feature (based on its word cloud). An example of the positive and negative word clouds for one such deep feature is shown in Figure 6a, and the resulting counterfactuals are in Table 6b (cf. Appendix F for details).

Counterfactuals generated in this manner successfully flip the sentiment label assigned by the sparse decision layer $73.1 \pm 3.0\%$ of the time. In contrast, such counterfactuals only have $52.2 \pm 4\%$ efficacy for

⁵We focus on this specific notion of “spurious correlations” as it is easy for humans to verify—cf. Appendix E.2 for details.



(a)

Original sentence	Counterfactual	Change in score
...something <i>likable</i> about the marquis...	...something <i>irritating</i> about the marquis...	0.73 → 0.34
<i>Slick</i> piece of cross- promotion	<i>Hype</i> piece of cross- promotion	0.73 → 0.34
A <i>marvel</i> like none you've seen	A <i>failure</i> like none you've seen	0.73 → 0.31

(b)

Figure 6: (a): Word cloud visualization for tokens that are positively/negatively correlated with the activation of a particular deep feature. (b): Using the wordclouds from (a), we can make word substitutions (as highlighted in green and red) to generate counterfactuals that change the model’s predicted sentiment (scores below 0.5 are predicted as negative).

the dense decision layer. This highlights that for models with sparse decision layers, it can be easier to automatically identify deep features that are causally-linked to model predictions.

ImageNet. We now leverage the annotations collected in Section 4.1 to generate counterfactuals for ImageNet classifiers. Concretely, we manually modify images to add or subtract input patterns identified by annotators and verify that they successfully flip the model’s prediction. Some representative examples are shown in Figure 7a. Here, we alter images from various ImageNet classes to have the pattern “chainlink fence” and “water”, so as to fool the sparse decision layer into recognizing them as “ballplayers” and “snorkels” respectively. We find that we are able to consistently change the prediction of the sparse decision layer (and in some cases its dense counterpart) by adding a pattern that was previously identified (cf. Section 4.1) to be a spurious correlation.

4.3 Misclassifications

Our final avenue for diagnosing unintended behaviors in models is through their misclassifications. Concretely, given an image for which the model makes an incorrect prediction (i.e., not the ground truth label as per the dataset), our goal is to pinpoint some aspects of the image that led to this error.

In the ImageNet setting, it turns out that over 30% of misclassifications made by the sparse decision layer can be attributed to a single deep feature—i.e., manually setting this “problematic” feature to zero fixes the erroneous prediction. For these instances, can humans understand why the problematic feature was triggered in the first place? Specifically, can they recognize the *pattern* in the input that caused the error?

To test this, we present annotators on MTurk with misclassified images. Without divulging the ground truth or predicted labels, we show annotators the top activated feature for each of the two classes via feature visualizations. We then ask annotators to select the patterns (i.e., feature visualizations) that match the image, and to choose one that is a better match for the image (cf. Appendix G.1 for details). As a control, we repeat the same task but replace the problematic feature with a randomly-chosen one.

For about 70% of the misclassified images, annotators select the top feature for the predicted class as being present in the image (cf. Table 8). In fact, annotators consider it a better match than the feature for the ground truth class 60% of the time. In contrast, they rarely select randomly-chosen features to be present in the image. Since annotators do not know what the underlying classes are, the high fraction of selections for the problematic feature indicates that annotators actually believe this pattern is present in the image.

We present sample misclassifications validated by annotators in Figure 7b, along with the problematic features that led to them. Having access to this information can guide improvements in both models and datasets. For instance, model designers might consider augmenting the training data with examples of “maracas” without “red tips” to correct the second error in Figure 7b. In Appendix G.3, we further discuss how sparse decision layers can provide insight into inter-class model confusion matrices.



Figure 7: (a) Counterfactual images for ImageNet. We manually modify samples (*top row*) to contain the patterns “chainlink fence” and “water”, which annotators deem (cf. Section 4.1) to be spuriously correlated with the classes “ballplayer” and “snorkel” respectively. We find that these counterfactuals (*bottom row*) succeed in flipping the prediction of the model with a sparse decision layer to the desired class. (b) Examples of misclassified ImageNet images for which annotators deem the top activated feature for the predicted class (*rightmost column*) as a better match than the top activated feature for the ground truth class (*middle column*).

Features	Matches image	Best match
Prediction	70.70% \pm 3.62%	60.12% \pm 3.77%
Random	16.63% \pm 2.91%	10.58% \pm 2.35%

Table 8: Fraction of misclassified images for which annotators select the top feature of the predicted class to: (i) match the given image and (ii) be a better match than the top feature for the ground truth class. As a baseline, we also evaluate annotator selections when the top feature for the predicted class is replaced by a randomly-chosen one.

5 Related Work

We now discuss prior work in interpretability and generalized linear models. Due to the large body of work in both fields, we limit the discussion to closely-related studies.

Interpretability tools. There have been extensive efforts towards post-hoc interpretability tools for deep networks. Feature attribution methods provide insight into model predictions for a specific input instance. These include saliency maps [SVZ13; Smi+17; STY17], surrogate models to interpret local decision boundaries [RSG16a], and finding influential [KL17], prototypical [KKK16], or counterfactual inputs [Goy+19a]. However, as noted by various recent studies, these local attributions can be easy to fool [GAZ19; Sla+20] or may otherwise fail to capture global aspects of model behavior [STY17; Ade+18; Ade+20; LM20]. Several methods have been proposed to interpret hidden units within vision networks, for example by generating feature visualizations [Erh+09; Yos+15; Ngu+16; OMS17] or assigning semantic concepts to them [Bau+17; Bau+20]. Our work is complementary to these methods as we use them as primitives to probe sparse decision layers. Another related line of work is that on concept-based explanations, which seeks to explain the behavior of deep networks in terms of high-level concepts [Kim+18; Gho+19; Yeh+20]. One of the drawbacks of these methods is that the detected concepts need not be causally linked to the model’s predictions [Goy+19b]. In contrast, in our approach, the identified high-level concepts, i.e., the deep features used by the sparse

decision layer, entirely determine the model’s behavior.

Most similar is the recent work by [Wan+20], which proposes fitting a decision tree on a deep feature representation. Network decisions are then explained in terms of semantic descriptions for nodes along the decision path. Wan et al. [Wan+20] rely on heuristics for fitting and labeling the decision tree, that require an existing domain-specific hierarchy (e.g., WordNet), causing it to be more involved and limited in its applicability than our approach.

Regularized GLMs and gradient methods. Estimating GLMs with convex penalties has been studied extensively. Algorithms for efficiently computing regularization paths include least angle regression for LASSO [Efr+04] and path following algorithms [PH07] for ℓ_1 regularized GLMs. The widely-used R package `glmnet` by Friedman, Hastie, and Tibshirani [FHT10] provides an efficient coordinate descent-based solver for GLMs with elastic net regularization, and attains state-of-the-art solving times on CPU-based hardware. Unlike our approach, this library is best suited for problems with few examples or features, and is not directly amenable to GPU acceleration. Our solver also builds off a long line of work in variance reduced proximal gradient methods [JZ13; DBLJ14; GGS19], which have stronger theoretical convergence rates when compared to stochastic gradient descent.

6 Conclusion

We demonstrate how fitting sparse linear models over deep representations can result in more debuggable models, and provide a diverse set of scenarios showcasing the usage of this technique in practice. The simplicity of our approach allows it to be broadly applicable to any deep network with a final linear layer, and may find uses beyond the language and vision settings considered in this paper.

Furthermore, we have created a number of human experiments for tasks such as testing model simulatability, detecting spurious correlations and validating misclassifications. Although primarily used in the context of evaluating the sparse decision layer, the design of these experiments may be of independent interest.

Finally, we recognize that while deep networks are popular within machine learning and artificial intelligence settings, linear models continue to be widely used in other scientific fields. We hope that the development and release of our elastic net solver will find broader use in the scientific community for fitting large scale sparse linear models in contexts beyond deep learning.

Acknowledgements

We thank Dimitris Tsipras for helpful discussions.

Work supported in part by the Google PhD Fellowship, Open Philanthropy, and NSF grants CCF-1553428 and CNS-1815221. This material is based upon work supported by the Defense Advanced Research Projects Agency (DARPA) under Contract No. HR001120C0015. Research was sponsored by the United States Air Force Research Laboratory and the United States Air Force Artificial Intelligence Accelerator and was accomplished under Cooperative Agreement Number FA8750-19-2-1000. The views and conclusions contained in this document are those of the authors and should not be interpreted as representing the official policies, either expressed or implied, of the United States Air Force or the U.S. Government. The U.S. Government is authorized to reproduce and distribute reprints for Government purposes notwithstanding any copyright notation herein.

References

- [Ade+18] Julius Adebayo et al. “Sanity checks for saliency maps”. In: *Neural Information Processing Systems (NeurIPS)*. 2018.
- [Ade+20] Julius Adebayo et al. “Debugging Tests for Model Explanations”. In: 2020.
- [Bau+17] David Bau et al. “Network dissection: Quantifying interpretability of deep visual representations”. In: *Computer Vision and Pattern Recognition (CVPR)*. 2017.

- [Bau+20] David Bau et al. “Understanding the role of individual units in a deep neural network”. In: *Proceedings of the National Academy of Sciences (PNAS)* (2020).
- [Bla+20] Davis Blalock et al. “What is the state of neural network pruning?”. In: *arXiv preprint arXiv:2003.03033* (2020).
- [Bor+19] Daniel Borkan et al. “Nuanced metrics for measuring unintended bias with real data for text classification”. In: *Companion Proceedings of The 2019 World Wide Web Conference*. 2019, pp. 491–500.
- [BSR20] Solon Barocas, Andrew D Selbst, and Manish Raghavan. “The hidden assumptions behind counterfactual explanations and principal reasons”. In: *Proceedings of the 2020 Conference on Fairness, Accountability, and Transparency*. 2020.
- [BVA20] Alceu Bissoto, Eduardo Valle, and Sandra Avila. “Debiasing Skin Lesion Datasets and Models? Not So Fast”. In: *Proceedings of the IEEE/CVF Conference on Computer Vision and Pattern Recognition Workshops*. 2020, pp. 740–741.
- [BVHP18] Sara Beery, Grant Van Horn, and Pietro Perona. “Recognition in terra incognita”. In: *European Conference on Computer Vision (ECCV)*. 2018.
- [DBLJ14] Aaron Defazio, Francis Bach, and Simon Lacoste-Julien. “SAGA: A fast incremental gradient method with support for non-strongly convex composite objectives”. In: *Advances in neural information processing systems (NeurIPS)*. 2014.
- [Den+09] Jia Deng et al. “Imagenet: A large-scale hierarchical image database”. In: *Computer Vision and Pattern Recognition (CVPR)*. 2009.
- [Dev+18] Jacob Devlin et al. “Bert: Pre-training of deep bidirectional transformers for language understanding”. In: *arXiv preprint arXiv:1810.04805* (2018).
- [Efr+04] Bradley Efron et al. “Least angle regression”. In: *The Annals of statistics* (2004).
- [Eng+19] Logan Engstrom et al. “Adversarial Robustness as a Prior for Learned Representations”. In: *ArXiv preprint arXiv:1906.00945*. 2019.
- [Erh+09] Dumitru Erhan et al. “Visualizing higher-layer features of a deep network”. In: (2009).
- [FHT10] Jerome Friedman, Trevor Hastie, and Rob Tibshirani. “Regularization paths for generalized linear models via coordinate descent”. In: *Journal of statistical software* (2010).
- [GAZ19] Amirata Ghorbani, Abubakar Abid, and James Zou. “Interpretation of neural networks is fragile”. In: *AAAI Conference on Artificial Intelligence (AAAI)*. 2019.
- [GGS19] Nidham Gazagnadou, Robert M Gower, and Joseph Salmon. “Optimal mini-batch and step sizes for SAGA”. In: *arXiv preprint arXiv:1902.00071* (2019).
- [Gho+19] Amirata Ghorbani et al. “Towards automatic concept-based explanations”. In: *arXiv preprint arXiv:1902.03129* (2019).
- [Goy+19a] Yash Goyal et al. “Counterfactual visual explanations”. In: *arXiv preprint arXiv:1904.07451* (2019).
- [Goy+19b] Yash Goyal et al. “Explaining classifiers with causal concept effect (cace)”. In: *arXiv preprint arXiv:1907.07165* (2019).
- [Han+15] Song Han et al. “Learning both weights and connections for efficient neural networks”. In: *arXiv preprint arXiv:1506.02626* (2015).
- [Has+07] Trevor Hastie et al. “Forward stagewise regression and the monotone lasso”. In: *Electronic Journal of Statistics* 1 (2007), pp. 1–29.
- [He+16] Kaiming He et al. “Deep Residual Learning for Image Recognition”. In: *Conference on Computer Vision and Pattern Recognition (CVPR)*. 2016.
- [HMD16] Song Han, Huizi Mao, and William J. Dally. “Deep Compression: Compressing Deep Neural Network with Pruning, Trained Quantization and Huffman Coding”. In: *International Conference on Learning Representations (ICLR)*. 2016.

- [HS93] Babak Hassibi and David Stork. "Second order derivatives for network pruning: Optimal Brain Surgeon". In: *Advances in Neural Information Processing Systems*. 1993.
- [Ily+19] Andrew Ilyas et al. "Adversarial Examples Are Not Bugs, They Are Features". In: *Neural Information Processing Systems (NeurIPS)*. 2019.
- [JZ13] Rie Johnson and Tong Zhang. "Accelerating stochastic gradient descent using predictive variance reduction". In: *Advances in neural information processing systems* 26 (2013), pp. 315–323.
- [Kim+18] Been Kim et al. "Interpretability beyond feature attribution: Quantitative testing with concept activation vectors (tcav)". In: *International conference on machine learning (ICML)*. 2018.
- [KKK16] Been Kim, Rajiv Khanna, and Oluwasanmi O Koyejo. "Examples are not enough, learn to criticize! criticism for interpretability". In: *Advances in neural information processing systems (NeurIPS)*. 2016.
- [KL17] Pang Wei Koh and Percy Liang. "Understanding Black-box Predictions via Influence Functions". In: *ICML*. 2017.
- [LDS90] Yann LeCun, John Denker, and Sara Solla. "Optimal Brain Damage". In: *Advances in Neural Information Processing Systems (NeurIPS)*. Morgan-Kaufmann, 1990.
- [Li+16] Hao Li et al. "Pruning filters for efficient convnets". In: *arXiv preprint arXiv:1608.08710* (2016).
- [Lip18] Zachary C Lipton. "The Mythos of Model Interpretability: In machine learning, the concept of interpretability is both important and slippery." In: (2018).
- [LM20] Matthew L Leavitt and Ari Morcos. "Towards falsifiable interpretability research". In: *arXiv preprint arXiv:2010.12016* (2020).
- [Mad+18] Aleksander Madry et al. "Towards deep learning models resistant to adversarial attacks". In: *International Conference on Learning Representations (ICLR)*. 2018.
- [Ngu+16] Anh Nguyen et al. "Synthesizing the preferred inputs for neurons in neural networks via deep generator networks". In: *Neural Information Processing Systems (NeurIPS)*. 2016.
- [OMS17] Chris Olah, Alexander Mordvintsev, and Ludwig Schubert. "Feature Visualization". In: *Distill*. 2017.
- [PH07] Mee Young Park and Trevor Hastie. "L1-regularization path algorithm for generalized linear models". In: *Journal of the Royal Statistical Society: Series B (Statistical Methodology)* (2007).
- [RSG16a] Marco Tulio Ribeiro, Sameer Singh, and Carlos Guestrin. "" Why should I trust you?" Explaining the predictions of any classifier". In: *International Conference on Knowledge Discovery and Data Mining (KDD)*. 2016.
- [RSG16b] Marco Tulio Ribeiro, Sameer Singh, and Carlos Guestrin. ""Why Should I Trust You?": Explaining the Predictions of Any Classifier". In: *International Conference on Knowledge Discovery and Data Mining (KDD)*. 2016.
- [Rus+15] Olga Russakovsky et al. "ImageNet Large Scale Visual Recognition Challenge". In: *International Journal of Computer Vision (IJCV)*. 2015.
- [Sal+20] Hadi Salman et al. "Do Adversarially Robust ImageNet Models Transfer Better?" In: *Advances in Neural Information Processing Systems (NeurIPS)*. 2020.
- [Sla+20] Dylan Slack et al. "Fooling lime and shap: Adversarial attacks on post hoc explanation methods". In: *Proceedings of the AAAI/ACM Conference on AI, Ethics, and Society*. 2020.
- [Smi+17] D. Smilkov et al. "SmoothGrad: removing noise by adding noise". In: *ICML workshop on visualization for deep learning*. 2017.
- [Soc+13] Richard Socher et al. "Recursive deep models for semantic compositionality over a sentiment treebank". In: *Proceedings of the 2013 conference on empirical methods in natural language processing*. 2013, pp. 1631–1642.
- [STY17] Mukund Sundararajan, Ankur Taly, and Qiqi Yan. "Axiomatic attribution for deep networks". In: *International Conference on Machine Learning (ICML)*. 2017.

- [SVZ13] Karen Simonyan, Andrea Vedaldi, and Andrew Zisserman. “Deep inside convolutional networks: Visualising image classification models and saliency maps”. In: *arXiv preprint arXiv:1312.6034* (2013).
- [Tib94] Robert Tibshirani. “Regression Shrinkage and Selection Via the Lasso”. In: *Journal of the Royal Statistical Society, Series B*. 1994.
- [Tsi+19] Dimitris Tsipras et al. “Robustness May Be at Odds with Accuracy”. In: *International Conference on Learning Representations (ICLR)*. 2019.
- [Tsi+20] Dimitris Tsipras et al. “From ImageNet to Image Classification: Contextualizing Progress on Benchmarks”. In: *International Conference on Machine Learning (ICML)*. 2020.
- [TW17] Ryan Tibshirani and Larry Wasserman. “Sparsity, the Lasso, and Friends”. In: *Lecture notes from “Statistical Machine Learning,” Carnegie Mellon University, Spring* (2017).
- [USL19] Berk Ustun, Alexander Spangher, and Yang Liu. “Actionable recourse in linear classification”. In: *Proceedings of the Conference on Fairness, Accountability, and Transparency*. 2019.
- [Wan+20] Alvin Wan et al. “NBDT: neural-backed decision trees”. In: *arXiv preprint arXiv:2004.00221* (2020).
- [WTD17] Ellery Wulczyn, Nithum Thain, and Lucas Dixon. “Ex machina: Personal attacks seen at scale”. In: *Proceedings of the 26th International Conference on World Wide Web*. 2017, pp. 1391–1399.
- [Xia+20] Kai Xiao et al. “Noise or signal: The role of image backgrounds in object recognition”. In: *arXiv preprint arXiv:2006.09994* (2020).
- [Yeh+20] Chih-Kuan Yeh et al. “On Completeness-aware Concept-Based Explanations in Deep Neural Networks”. In: *Advances in Neural Information Processing Systems (NeurIPS)* (2020).
- [Yos+15] Jason Yosinski et al. “Understanding neural networks through deep visualization”. In: *arXiv preprint arXiv:1506.06579*. 2015.
- [ZH05] Hui Zou and Trevor Hastie. “Regularization and variable selection via the elastic net”. In: *Journal of the royal statistical society: series B (statistical methodology)* (2005).
- [Zho+17] Bolei Zhou et al. “Places: A 10 million image database for scene recognition”. In: *IEEE transactions on pattern analysis and machine intelligence* (2017).

A SAGA-based solver for generalized linear models

In this section, we describe in further detail our solver for learning regularized GLMs in relation to existing work. Note that many of the components underlying our solver have been separately studied in prior work. However, we are the first to effectively combine them in a way that allows for GPU-accelerated fitting of GLMs at ImageNet-scale. The key algorithmic primitives we leverage to this end are variance reduced optimization methods and path algorithms for GLMs.

Specifically, our solver uses a mini-batch derivative of the SAGA algorithm [GGS19], which belongs to a class of a variance reduced proximal gradient methods. These approaches have several benefits: a) they are easily parallelizable via GPU, b) they enjoy faster convergence rates than stochastic gradient methods, and c) they require minimal tuning and can converge with a fixed learning rate.

Algorithm 1 provides a step-by-step description of our solver. Here, the proximal operator for elastic net regularization is

$$\text{Prox}_{\lambda_1, \lambda_2}(\beta) = \begin{cases} \frac{\beta - \lambda_1}{1 + \lambda_2} & \text{if } \beta > \lambda_1 \\ \frac{\beta + \lambda_1}{1 + \lambda_2} & \text{if } \beta < -\lambda_1 \\ 0 & \text{otherwise} \end{cases} \quad (4)$$

Table for storing gradients Note that the SAGA algorithm requires saving the gradients of the model for each individual example. For ImageNet-sized problems, this requires a prohibitive amount of memory, as both the number of examples (>1 million) and the size of the gradient (of the linear model) are large.

It turns out that for linear models with k outputs, it is actually possible to store all of the necessary gradient information for a single example in a vector of size k —as demonstrated by Defazio, Bach, and Lacoste-Julien [DBLJ14]. The key idea behind this approach is that rather than storing the full gradient step $(x_i^T \beta + \beta_0 - y_i)x_i$, we can instead just store the scalar $a_i = (x_i^T \beta + \beta_0 - y_i)$ per output (i.e., a vector of length k in the case of multiple outputs). Thus, for a dataset with n examples, this reduces the memory requirements of the gradient table to $O(nk)$. For ImageNet, we find that the entire table easily fits within GPU memory limits.

There is one caveat here: in order to use this memory trick, it is necessary to incorporate the ℓ_2 regularization from the elastic net into the proximal operator. This is precisely why we use the proximal operator of the elastic net, rather than of the ℓ_1 regularization. Unfortunately, this means that the smooth part of the objective (i.e. the part not used in the proximal operator) is no longer guaranteed to be strongly convex, and so the theoretical analysis of Gazagnadou, Gower, and Salmon [GGS19] no longer strictly applies. Nonetheless, we find that these variance reduced methods can still provide strong practical convergence rates in this setting without requiring much tuning of batch sizes or learning rates.

Stopping criterion We implement two simple stopping criteria, which both take in a tolerance level ε_{tol} . The first is a gradient-based stopping criteria, which terminates when:

$$\sqrt{\|\beta^{i+1} - \beta^i\|_2^2 + \|\beta_0^{i+1} - \beta_0^i\|_2^2} \leq \varepsilon_{\text{tol}}$$

Intuitively, this stops when the change in the estimated coefficients is small. Our second stopping criteria is more conservative and uses a longer search horizon, and stops when the training loss has not improved by more than ε_{tol} for more than T epochs for some T , which we call the lookbehind stopping criteria.

In practice, we find that the gradient-based stopping criteria with $\varepsilon_{\text{tol}} = 10^{-4}$ is sufficient for most cases (i.e. the solver has converged sufficiently such that the number of non-zero entries will no longer change). For significantly larger problems such as ImageNet, where individual batch sizes can have much larger variability in progressing the training objective, we find that the lookbehind stopping criteria is sufficient with $\varepsilon_{\text{tol}} = 10^{-4}$ and $T = 5$.

Relation of the solver to existing work We now discuss how our solver borrows and differs from existing work. First, note that the original SAGA algorithm [DBLJ14] analyzes the regularized form but updates its gradient estimate with one sample at a time, which is not amenable to GPU parallelism. On the other hand,

Algorithm 1 GPU-accelerated solver for the elastic net for a step size γ and regularization parameters λ, α

```

1: Initialize table of scalars  $a'_i = 0$  for  $i \in [n]$ 
2: Initialize average gradient of table  $g_{avg} = 0$  and  $g_{0avg} = 0$ 
3: for minibatch  $B \subset [n]$  do
4:   for  $i \in B$  do
5:      $a_i = x_i^T \beta + \beta_0 - y_i$ 
6:      $g_i = a_i \cdot x_i$  // calculate new gradient information
7:      $g'_i = a'_i \cdot x_i$  // calculate stored gradient information
8:   end for
9:    $g = \frac{1}{|B|} \sum_{i \in B} g_i$ 
10:   $g' = \frac{1}{|B|} \sum_{i \in B} g'_i$ 
11:   $g_0 = \frac{1}{|B|} \sum_{i \in B} a_i$ 
12:   $g'_0 = \frac{1}{|B|} \sum_{i \in B} a'_i$ 
13:   $\beta = \beta - \gamma(g - g' + g_{avg})$ 
14:   $\beta_0 = \beta_0 - \gamma(g_0 - g'_0 + g_{0avg})$ 
15:   $\beta = \text{Prox}_{\gamma\lambda\alpha, \gamma\lambda(1-\alpha)}(\beta)$ 
16:  for  $i \in B$  do
17:     $a'_i = a_i$  // update table
18:     $g_{avg} = g_{avg} + \frac{|B|}{n}(g - g')$  // update average
19:     $g_{0avg} = g_{0avg} + \frac{|B|}{n}(g_0 - g'_0)$ 
20:  end for
21: end for

```

Gazagnadou, Gower, and Salmon [GGS19] analyze a minibatch variant of SAGA but without regularization. In our solver, we use a straightforward adaptation of minibatch SAGA to its regularized equivalent by including a proximal step for the elastic net regularization after the gradient step.

To compute the regularization paths, we closely follow the framework of Friedman, Hastie, and Tibshirani [FHT10]. Specifically, we compute solutions for a decreasing sequence of regularization, using the solution of the previous regularization as a warm start for the next. The maximum regularization value which fits only the bias term is calculated as the fixed point of the coordinate descent iteration as

$$\lambda_{max} = \max_j \frac{1}{N\alpha} \left| \sum_{i=1}^n x_{ij} y_i \right| \quad (5)$$

and scheduled down to $\lambda_{min} = \varepsilon \lambda_{max}$ over a sequence of K values on a log scale, as done by Friedman, Hastie, and Tibshirani [FHT10]. Typical suggested values are to take $K = 100$ and $\varepsilon = 0.001$, which are what we use in all of our experiments. For extensions to logistic and multinomial regression, we refer the reader to Friedman, Hastie, and Tibshirani [FHT10], and note that our approach is the same but substituting our SAGA-based solver in lieu of the coordinate descent-based solver.

A.1 Timing Experiments

In this section, we discuss how the runtime of our solver scales with the problem size. To be able to compare our solver with existing approaches, the experiments performed here are at a smaller scale than those in the main body of the paper.

Problem setting & hyperparameters. The problem we examine is that of fitting a linear decision layer for the CIFAR-10 dataset using the deep feature representation of an ImageNet-trained ResNet-50 (2048-dimensional features). We then vary the number of training examples (from 1k to 50k) and fit an elastic net regularized GLM using various methods. We compare `glmnet` (state-of-the-art, coordinate descent-based solver) on a 9th generation Intel Core i7 with 6 cores clocked at 2.6Ghz, and our approach `glm-saga` using a

Table 36: Runtime in minutes for glmnet and glm-saga for fitting a sparse decision layer on the CIFAR-10 dataset using deep representations (2048D) for a pre-trained ResNet-50. Here, we assess how the runtime of different solvers scales as a function of training data points.

Solver	Number of examples					
	1k	2k	3k	4k	5k	50k
glmnet	2	7	25	39	58	776
glm-saga	9	13	17	19	22	33

GeForce GTX 1080ti. We note that in these small-scale experiments, the graphics card remains at around 10-20% utilization, indicating that the problem size is too small to fully utilize the GPU.

We fix $\alpha = 0.99$, $\varepsilon = 10^{-4}$, set aside 10% of the training data for validation, and calculate regularization paths for $k = 100$ different values, which are the defaults for glmnet. For our approach, we additionally use a mini-batch size of 512, a learning rate of 0.1, and a tolerance level of 10^{-4} for the gradient-based stopping criteria.

Improvements in scalability As expected, on smaller problem instances with a couple thousand examples, glmnet is faster than our solver—cf. Table 36. This is largely due to the increased base running time of our solver—a consequence of gradient based methods requiring some time to converge. However, as the problem size grows, the runtime of glmnet increases rapidly, and exceeds the running time of glm-saga at 3,000 datapoints. For example, it takes almost 40 minutes to fit 4,000 data points with glmnet, an increase of 20x the running time for 4x the data relative to the running time for 1,000 data points. In contrast, our solver only needs 19 minutes to fit 4,000 datapoints, an increase of 2x the running time for 4x the data. Consequently, while glmnet takes a considerable amount of time to fit the full CIFAR10 problem size (50,000 datapoints)—nearly 13 hours—our solver can do the same in only 33 minutes. Notably, our solver can fit the regularization paths of the decision layer for the full ImageNet dataset (1 million examples with 2048 features) in approximately 6 hours.

Backpropagation libraries One more alternative to fitting linear models at scale is to use a standard autodifferentiation library such as PyTorch or Tensorflow. However, typical optimizers used in these libraries do not handle non-smooth regularizers well (i.e., the ℓ_1 penalty of the elastic net). In practice, these types of approaches must gradually schedule learning rates down to zero in order to converge, and take too long to compute regularization paths. For example, the fixed-feature transfer experiments from Salman et al. [Sal+20] takes approximately 4 hours to fit the same CIFAR10 timing experiment for a single regularization value. In contrast, the SAGA-based optimizers enables a flexible range of learning rates that can converge rapidly without needing to tune or decay the learning rate over time.

A.2 Elastic net, ℓ_1 , and ℓ_2 regularization

The elastic net is known to combine the benefits of both ℓ_1 and ℓ_2 regularization for linear models. The ℓ_1 regularization, often seen in the LASSO, primarily provides sparsity in the solution. The ℓ_2 regularization, often seen as ridge regression, brings improved performance, a unique solution via strong convexity, and a grouping effect of similar neurons. Due to this last property of ℓ_2 regularization, highly correlated features will become non-zero at the same time over the regularization path. The elastic net combines all of these strengths, and we refer the reader to Tibshirani and Wasserman [TW17] for further discussion on the interaction between elastic net, ℓ_1 , and ℓ_2 .

A.3 Feature ordering

In the main body of the paper, we utilized regularization paths obtained via elastic net to obtain a sparse decision layer over deep features. We now discuss an additional use case of regularization paths—as a means

to assess relative (deep) feature importance within the decision layer of a standard deep network. Such an ordering could, for instance, provide an alternative criteria for feature selection in "feature-highlighting" explanations [BSR20].

The underlying mechanism that allows us to do this is the ℓ_1 regularization in the elastic net, which imposes sparsity properties on the coefficients of the resulting linear model [Tib94]. Specifically, the coefficients for each feature become non-zero at discrete points in the regularization path, as λ tends to zero. Informally, one can view features that are assigned non-zero coefficients earlier as being more useful from an accuracy standpoint, given the sparsity regularization.

Consequently, the order in which (deep) features are incorporated into the sparse decision layers, within the regularization path, may shed light on their relative utility within the *standard* deep network. In Figures 12- 15, we illustrate regularization paths along with the derived feature ordering for standard and robust ResNet-50 classifiers trained on ImageNet and Places-10 datasets. For all the models, it appears that features that are incorporated earlier into the regularization path (for a class) are actually more semantically aligned with the corresponding object category.

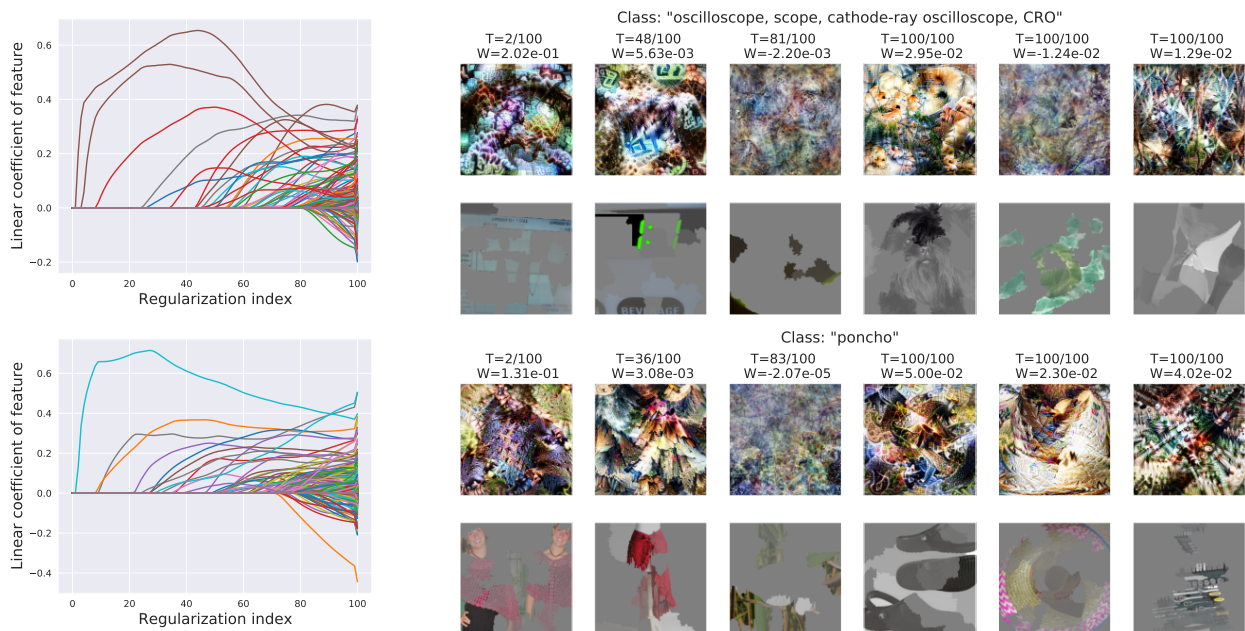


Figure 12: Sample regularization paths (*left*) and feature ordering (*right*) for sparse decision layers trained on deep features of a ResNet-50 classifier for two ImageNet classes. Regularization paths highlight when different deep features are incorporated into the decision layer as the sparsity regularization is reduced. Sample features (as feature visualizations and LIME superpixels) included into the decision layer at increasing regularization indices (T) are shown on the right.

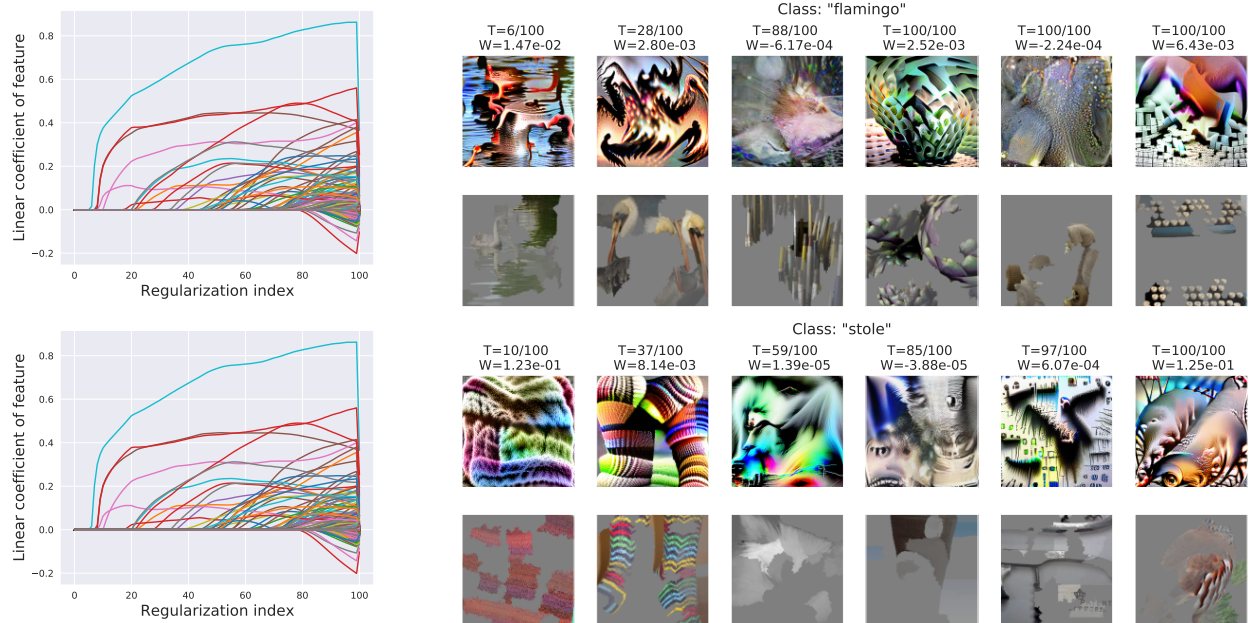


Figure 13: Sample regularization paths (*left*) and feature ordering (*right*) for sparse decision layers trained on deep features of a robust ResNet-50 classifier for two ImageNet classes. Regularization paths highlight when different deep features are incorporated into the decision layer as the sparsity regularization is reduced. Sample features (as feature visualizations and LIME superpixels) included into the decision layer at increasing regularization indices (T) are shown on the right.

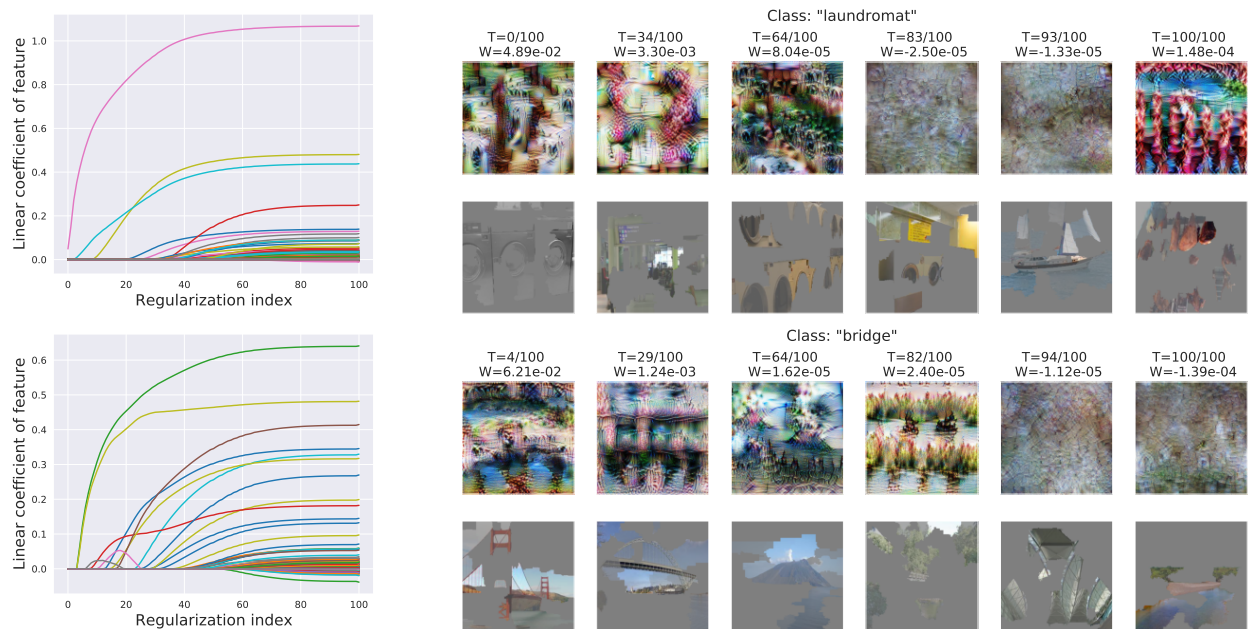


Figure 14: Sample regularization paths (*left*) and feature ordering (*right*) for sparse decision layers trained on deep features of a ResNet-50 classifier for two Places-10 classes. Regularization paths highlight when different deep features are incorporated into the decision layer as the sparsity regularization is reduced. Sample features (as feature visualizations and LIME superpixels) included into the decision layer at increasing regularization indices (T) are shown on the right.

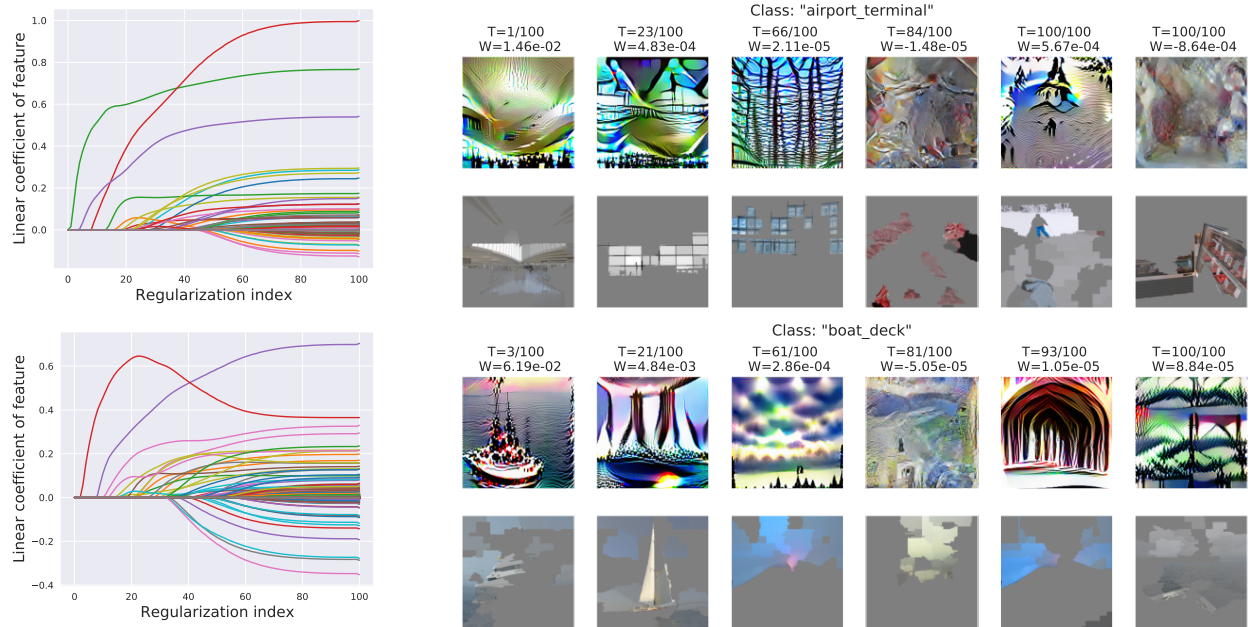


Figure 15: Sample regularization paths (*left*) and feature ordering (*right*) for sparse decision layers trained on deep features of a robust ResNet-50 classifier for two Places-10 classes. Regularization paths highlight when different deep features are incorporated into the decision layer as the sparsity regularization is reduced. Sample features (as feature visualizations and LIME superpixels) included into the decision layer at increasing regularization indices (T) are shown on the right.

B Feature interpretations

We now discuss in depth our procedure for generating feature interpretations for deep features in the vision and language settings.

B.1 Feature visualization

Feature visualization is a popular approach to interpret individual neurons within a deep network. Here, the objective is to synthesize inputs (via optimization in pixel space) that highly activate the neuron of interest. Unfortunately, for standard networks trained via empirical risk minimization, it is well-known that vanilla feature visualization—using just gradient descent in input space—fails to produce semantically-meaningful interpretations. In fact, these visualizations frequently suffer from artifacts and high frequency patterns [OMS17]. One cause for this could be the reliance of standard models on input features that are imperceptible or unintuitive, as has been noted in recent studies [Ily+19].

To mitigate this challenge, there has been a long line of work on defining modified optimization objectives to produce more meaningful feature visualizations [OMS17]. In this work, we use the Tensorflow-based Lucid library⁶ to produce feature visualizations for standard models. Therein, the optimization objective contains additional regularizations to penalize high-frequency changes in pixel space and to encourage transformation robustness. Further, gradient descent is performed in the Fourier basis to further discourage high-frequency input patterns. We defer the reader to Olah, Mordvintsev, and Schubert [OMS17] for a more complete presentation.

In contrast, a different line of work [Tsi+19; Eng+19] has shown that robust (adversarially-trained) models tend to have better feature representations than their standard counterparts. Thus, for robust models, gradient descent in pixel space is already sufficient to find semantically-meaningful feature visualizations.

B.2 LIME

Image superpixels. Traditionally, LIME is used to obtain instance-specific explanations—i.e., to identify the superpixels in a given test image that are most responsible for the model’s prediction. However, in our setting, we would like to obtain a global understanding of deep features, independent of specific test examples. Thus, we use the following two step-procedure to obtain LIME-based feature interpretations:

1. Rank test set images based on how strongly they activate the feature of interest. Then select the top- k (or conversely bottom- k) images as the most prototypical examples for positive (negative) activation of the feature.
2. Run LIME on each of these examples to identify relevant superpixels. At a high level, this involves performing linear regression to map image superpixels to the (normalized) activation of the deep feature (rather than the probability of a specific class as is typical).

Due to space constraints, we use $k = 1$ in all our figures. However, in our analysis, we found the superpixels identified with $k = 1$ to be representative of those obtained with higher values.

Word clouds for language models For language models, off-the-shelf neuron interpretability tools are somewhat more limited than their vision counterparts. Of the tools listed above, only LIME is used in the language domain to produce sentence-specific explanations. Similar to our methodology for vision models, we apply LIME to a given deep feature representation rather than the output neuron. However, rather than selecting prototypical images, we instead aggregate LIME explanations over the entire validation set.

Specifically, for a given feature, we average the LIME weighting for each word over all of the sentences that the word appears in. This allows us to identify words that strongly activate/deactivate the given feature globally over the entire validation set, which we then visualize using word clouds. In practice, since a word cloud has limited space, we provide the top 30 most highly weighted words to the word cloud generator. The exact procedure is shown in Algorithm 2, and we use the word cloud generator from https://github.com/amueller/word_cloud.

⁶<https://github.com/tensorflow/lucid>

Algorithm 2 Word cloud feature visualization for language models for a vocabulary V , a corpus w_{ij} for $i, j \in [m] \times [n]$ of m sentences with n words

```

1: for  $i = 1 \dots m$  do
2:    $\beta_i = \text{LIME}(w_i)$  // generate LIME explanation for each sentence
3: end for
4: for  $w \in V$  do
5:    $K_w = \sum_{ij:w=w_{ij}} 1$  // count number of occurrences of word
6:    $\hat{\beta}_w = \frac{1}{K_w} \sum_{ij:w=w_{ij}} \beta_{ij}$  // calculate average LIME explanation of word
7: end for
8: return Wordcloud( $\beta, V$ ) // generate word cloud for vocabulary  $V$  weighted by  $\beta$ 

```

C Datasets and Models

C.1 Datasets

We perform our experiments on the following widely-used vision and language datasets.

- ImageNet-1k [Den+09; Rus+15].
- Places-10: A subset of Places365 [Zho+17] containing the classes “airport terminal”, “boat deck”, “bridge”, “butcher’s shop”, “church-outdoor”, “hotel room”, “laundromat”, “river”, “ski slope” and “volcano”.
- Stanford Sentiment Treebank (SST) [Soc+13] with labels for “positive” and “negative” sentiment.
- Toxic Comments [WTD17] with labels for “toxic”, “severe toxic”, “obscene”, “threat”, “insult”, and “identity hate”.

Balancing the comment classification task. The toxic comments classification task has a highly unbalanced test set, and is largely skewed towards non-toxic comments. Consequently, the baseline accuracy for simply predicting the non-toxic label is often upwards of 90% on the unbalanced test set. To get a more interpretable and usable performance metric, we instead randomly subsample the test set to be balanced with 50% each of toxic and non-toxic comments from the corresponding toxicity category. Thus, the baseline accuracy for random chance for toxic comment classification in our experiments is 50%.

C.2 Models

We consider ResNet-50 [He+16] classifiers and BERT [Dev+18] models for vision and language tasks respectively. In the vision setting, we consider both standard and robust models [Mad+18].

Vision. All the models are trained for 90 epochs, weight decay $1e-4$ and momentum 0.9. We used a batch size of 512 for ImageNet and 128 for Places-10. The initial learning rate is 0.1 and is dropped by a factor of 10 every 30 epochs. The robust models were obtained using adversarial training with a ℓ_2 PGD adversary [Mad+18] with $\varepsilon = 3$, 3 attack steps and attack step size of $\frac{2 \times \varepsilon}{3}$.

Language. The language models are all pretrained and available from the HuggingFace library, and use the standard BERT base architecture. Specifically, the sentiment classification model is from <https://huggingface.co/barissayil/bert-sentiment-analysis-sst> and the toxic comment models (both Toxic-BERT and Debiased-BERT) come from <https://huggingface.co/unitary/toxic-bert>.

D Evaluating sparse decision layers

D.1 Trade-offs for all datasets

In Figure 16, we present an extended version of Figure 3a—including all the tasks and models we consider in both the vision and language setting. Each point on the curve corresponds to single linear classifier from the regularization path in Equation (3). Note that we include the (same) SST curve in both language plots for the Toxic and Debiased BERT models.

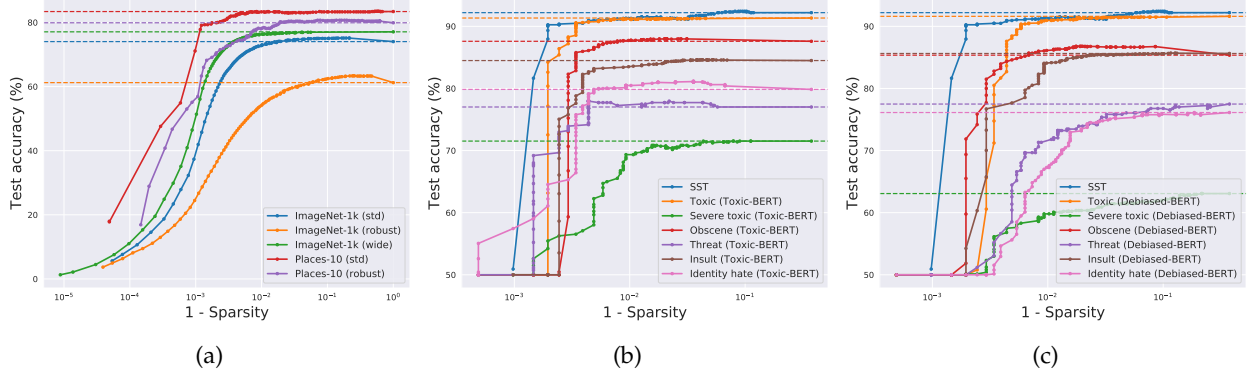


Figure 16: Sparsity vs. accuracy trade-offs of models with sparse decision layers for (a) vision and (b,c) language tasks.

D.1.1 Selecting a single sparse model

As discussed in Section 2.1, the elastic net yields a sequence of linear models—with varying accuracy and sparsity—also known as the regularization path. In practice, performance of these models on a hold-out validation set can be used to guide model selection based on application-specific criteria. In our experiments, we set aside 10% of the train set for this purpose.

Our model selection thresholds. For both vision and NLP tasks, we use the validation set to identify the sparsest decision layer, whose accuracy is no more than 5% lower on the validation set, compared to the best performing decision layer. As discussed in the paper, these thresholds are meant to be illustrative and can be varied depending on the specific application. We now visualize the per-class distribution of deep features for the sparse decision layers selected in Table 3b. (We omit the NLP tasks as they entail only two classes.)

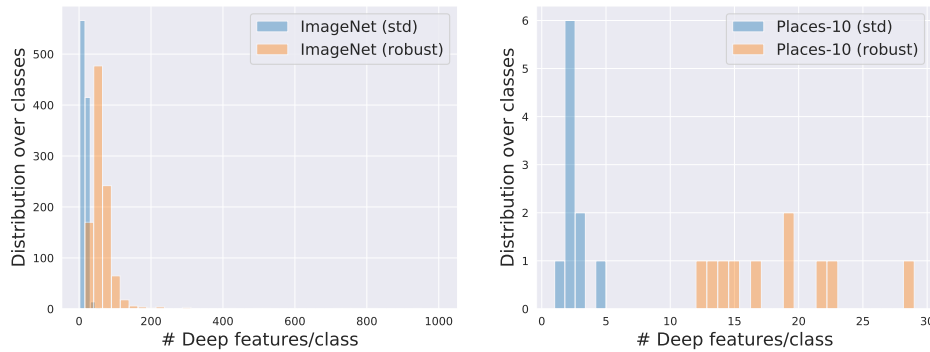


Figure 17: Distribution of the number of deep features used per class by sparse decision layers of vision models. Note that a standard (dense) decision layer uses all 2048 deep features to predict every class.

Table 37: Extended version of Table 3b: Comparison of the accuracy of dense/sparse decision layers when they are constrained to utilize only the top- k deep features (based on weight magnitude). We also show overall model accuracy, and the accuracy gained by using the remaining deep features.

Dataset/Model	k	Dense			Sparse		
		All	Top- k	Rest	All	Top- k	Rest
ImageNet (std)	10	74.03	58.46	55.22	72.24	69.78	10.84
ImageNet (wide, std)		77.07	72.42	48.75	73.48	73.45	0.91
ImageNet (robust)		61.23	28.99	34.65	59.99	45.82	19.83
Places-10 (std)	10	83.30	83.60	81.20	77.40	77.40	10.00
Places-10 (robust)		80.20	76.10	76.40	77.80	76.60	40.20
SST	5	91.51	53.21	91.17	90.71	90.48	50.92
Toxic-BERT (toxic)	5	83.33	55.35	57.87	82.47	82.33	50.00
Toxic-BERT (severe toxic)		71.53	50.00	50.14	67.57	50.00	50.00
Toxic-BERT (obscene)		80.41	50.03	50.00	77.32	72.39	50.00
Toxic-BERT (threat)		77.01	50.00	50.00	76.30	74.17	50.00
Toxic-BERT (insult)		72.72	50.00	50.00	77.14	75.80	50.00
Toxic-BERT (identity hate)		79.85	57.87	50.00	74.93	71.49	50.00
Debiased-BERT (toxic)	5	91.61	50.00	83.26	87.59	78.58	50.00
Debiased-BERT (severe toxic)		63.08	50.00	50.00	55.86	53.81	50.00
Debiased-BERT (obscene)		85.36	50.00	58.36	81.50	81.17	50.00
Debiased-BERT (threat)		77.49	50.00	50.00	68.96	50.00	50.00
Debiased-BERT (insult)		85.63	50.00	59.95	79.28	71.48	50.00
Debiased-BERT (identity hate)		76.12	50.00	50.84	71.98	50.00	50.00

D.2 Feature highlighting

In Table 37 we show an extended version of Table 3b, which now contains an additional wide ImageNet representation as well as 3 additional toxic comment categories for each toxic comment classifier. The overall test accuracy of a subset of these models (before sparsification) is under ‘Dense \rightarrow All’ in Figure 3b.

D.3 Additional comparisons of features

In Figure 16, we visualize additional deep features used by BERT models with sparse decision layers for the SST sentiment analysis task. Figures 17- 22 show feature interpretations of deep features used by ResNet-50 classifiers with sparse decision layers trained on ImageNet and Places-10. Due to space constraints, we limit the feature interpretations for vision models to (at most) five randomly-chosen deep features used by the dense/sparse decision layer in Figure 2b and Figures 17- 22. To allow for a fair comparison between the two decision layers, we sample these features as follows. Given a target class, we first determine the number of deep features (k) used by the sparse decision layer to recognize objects of that class. Then, for both decision layers, we randomly sample five deep features from the top- k highest weighted ones (for that class).

D.3.1 Language models



Figure 16: Additional SST word clouds visualizing the positive and negative activations for the top 5 features of the (a) sparse decision layer, (b) dense decision layer, and (c) additional randomly-selected features (positive or negative weighting is according to the dense decision layer). While the sparse model focuses on features that have clear positive and negative semantic meaning in their word clouds, the dense model and the other randomly-selected features are noticeably more mixed in sentiment.

D.3.2 Vision models

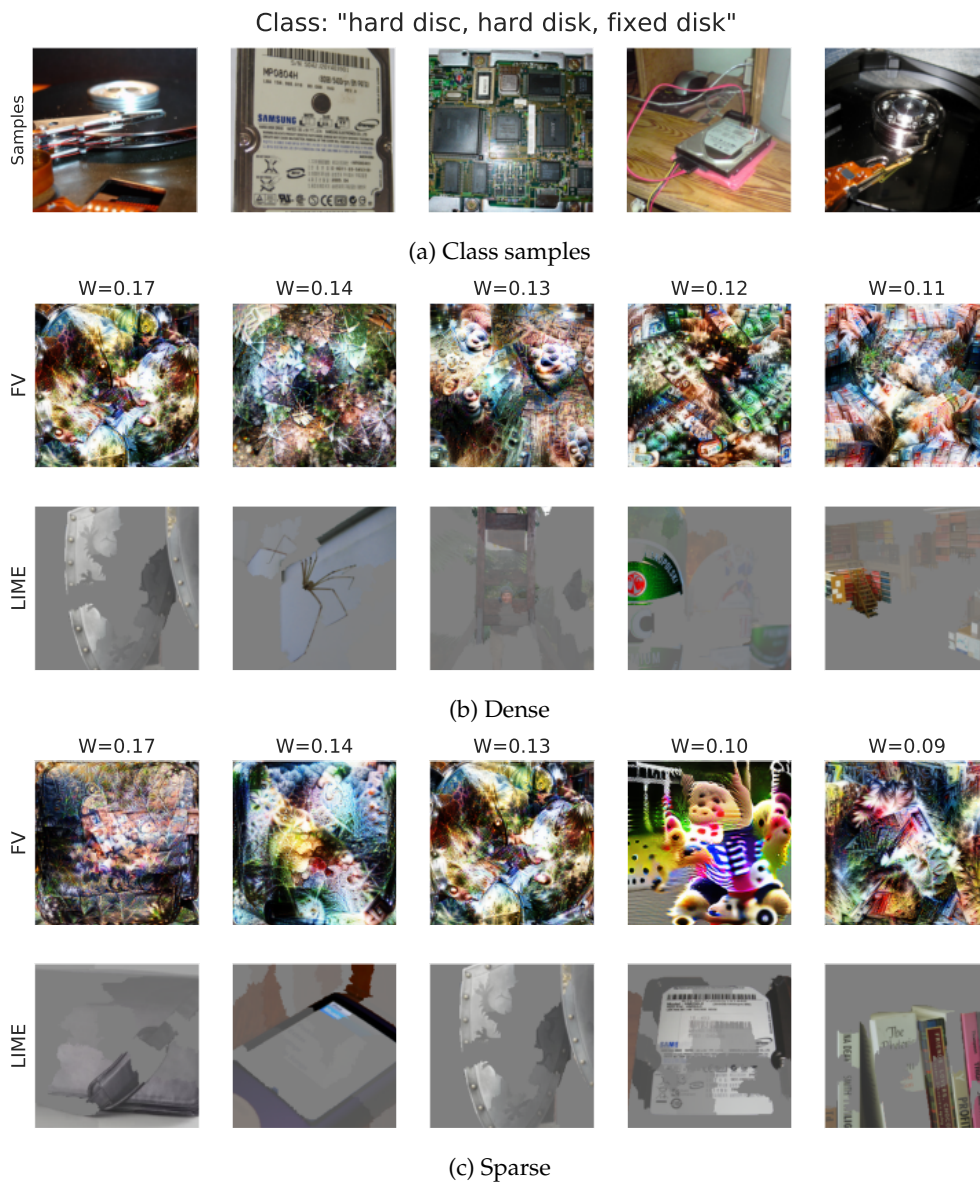
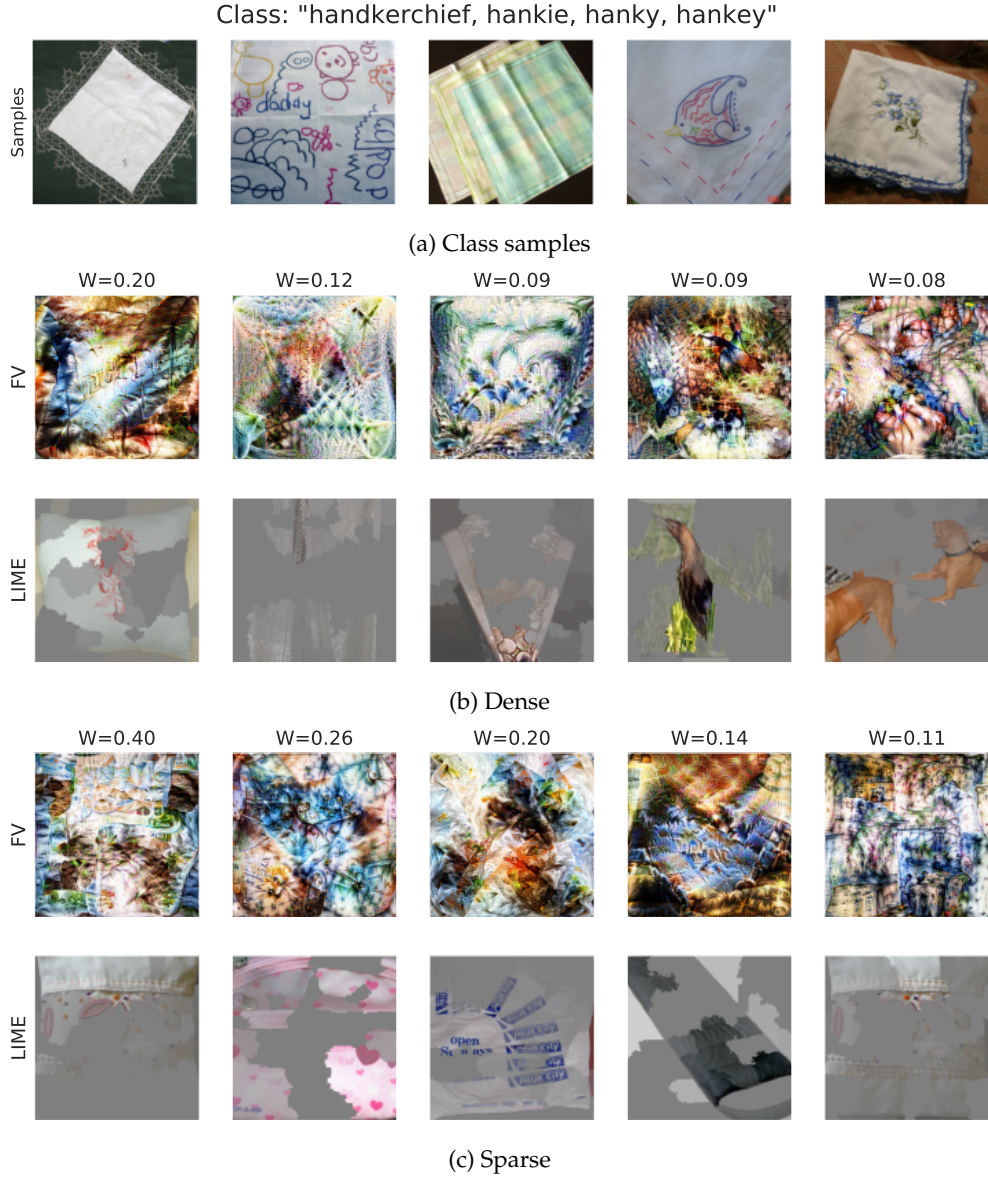


Figure 17: Deep features used by a standard ($\epsilon = 0$) ResNet-50 with dense (*middle*) and sparse decision layers (*bottom*) for a randomly-chosen ImageNet class. For each (deep) feature, we show its corresponding linear coefficient in the decision layer (W), along with feature interpretations in the form of feature visualizations (FV) and LIME superpixels.



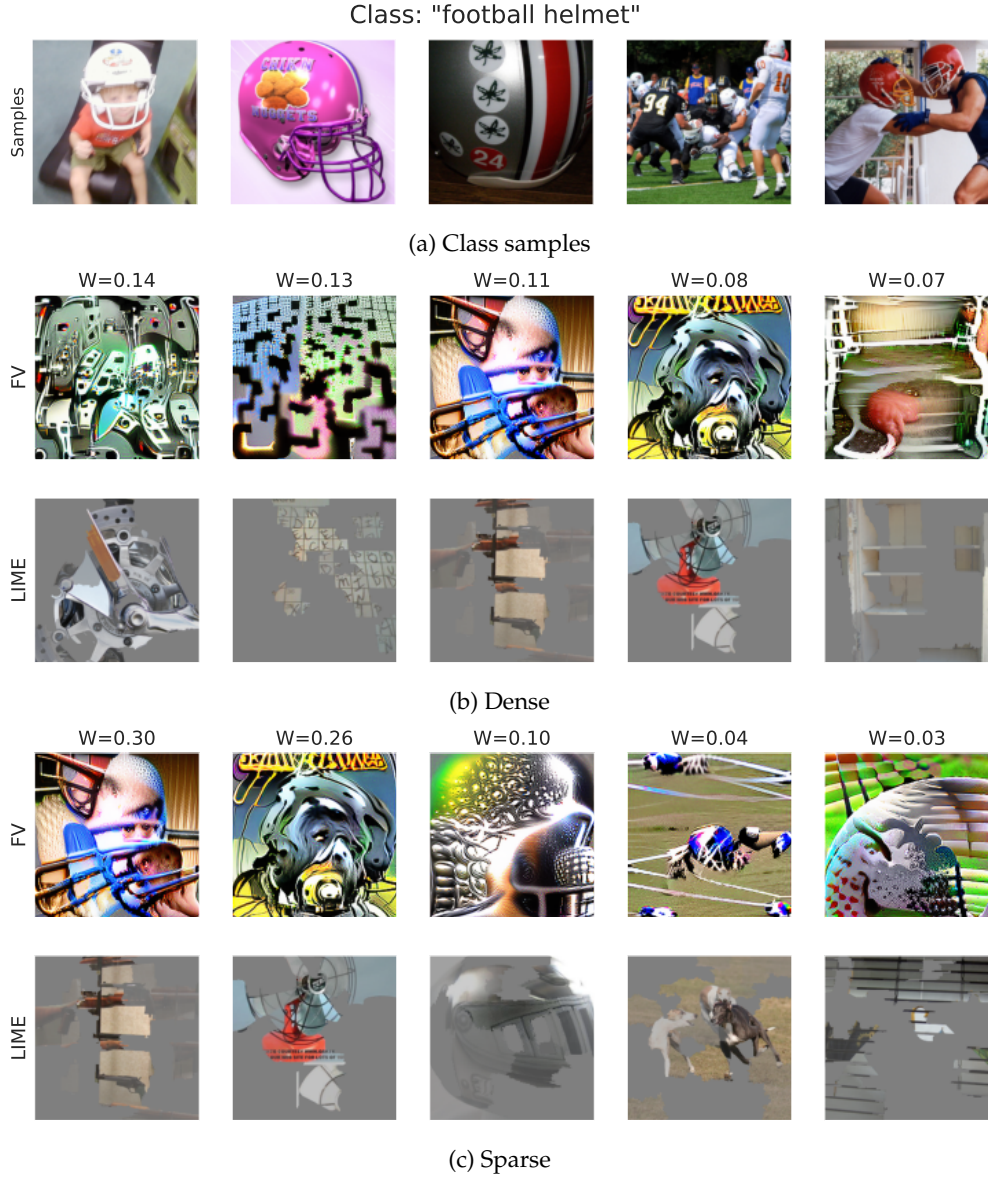


Figure 19: Deep features used by a adversarially-trained ($\epsilon = 3$) ResNet-50 with dense (*middle*) and sparse decision layers (*bottom*) for a randomly-chosen ImageNet class. For each (deep) feature, we show its corresponding linear coefficient in the decision layer (W), along with feature interpretations in the form of feature visualizations (FV) and LIME superpixels.

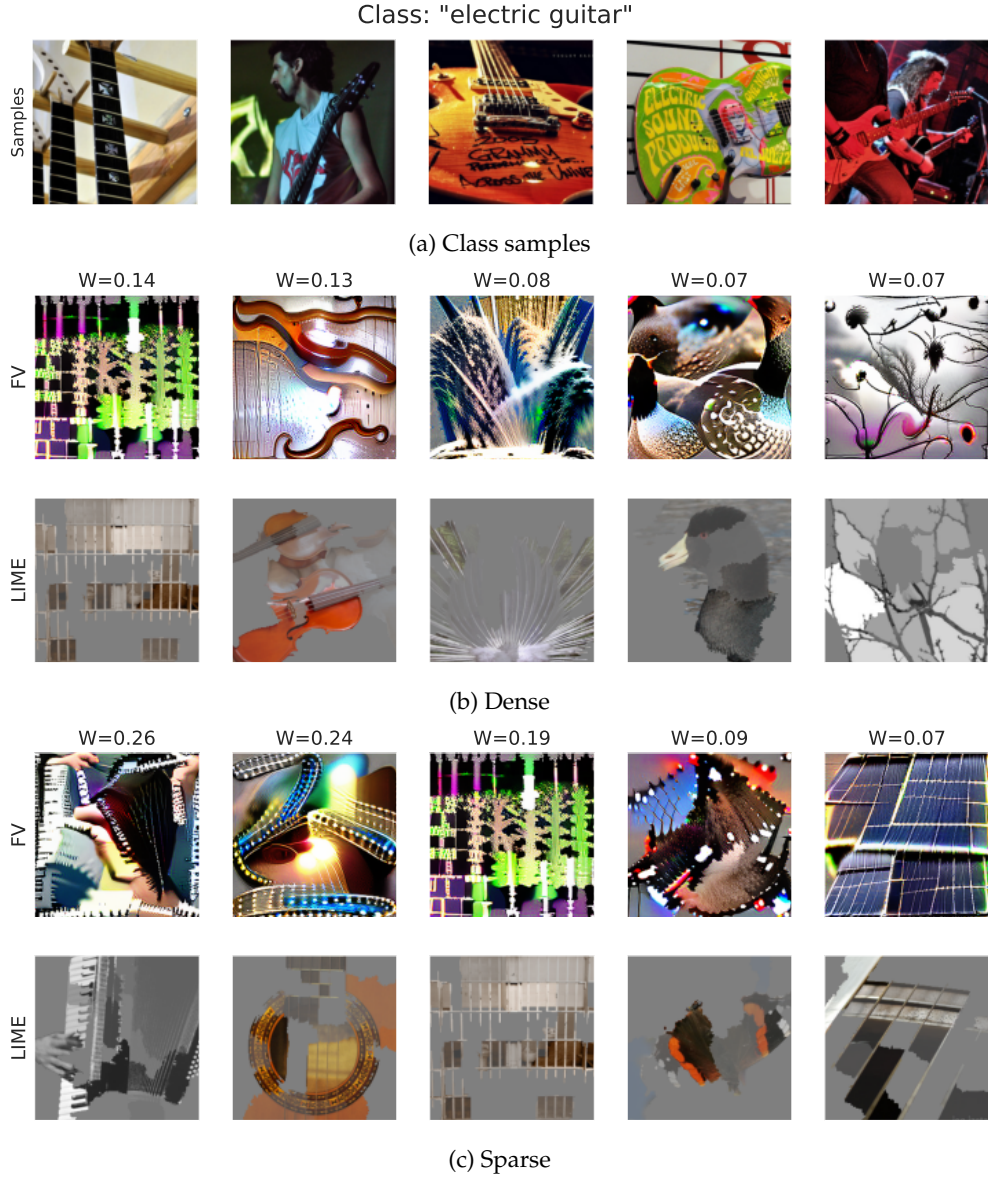
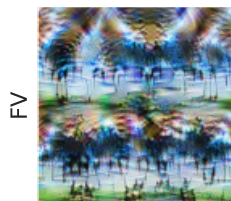


Figure 20: Deep features used by a adversarially-trained ($\epsilon = 3$) ResNet-50 with dense (*middle*) and sparse decision layers (*bottom*) for a randomly-chosen ImageNet class. For each (deep) feature, we show its corresponding linear coefficient in the decision layer (W), along with feature interpretations in the form of feature visualizations (FV) and LIME superpixels.



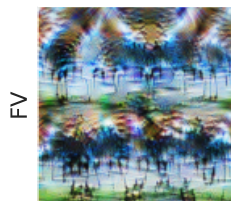
(a) Class samples

$W=0.81$



(b) Dense

$W=1.00$



(c) Sparse

Figure 21: Deep features used by a standard ($\epsilon = 0$) ResNet-50 with dense (*middle*) and sparse decision layers (*bottom*) for a randomly-chosen Places-10 class. For each (deep) feature, we show its corresponding linear coefficient in the decision layer (W), along with feature interpretations in the form of feature visualizations (FV) and LIME superpixels.

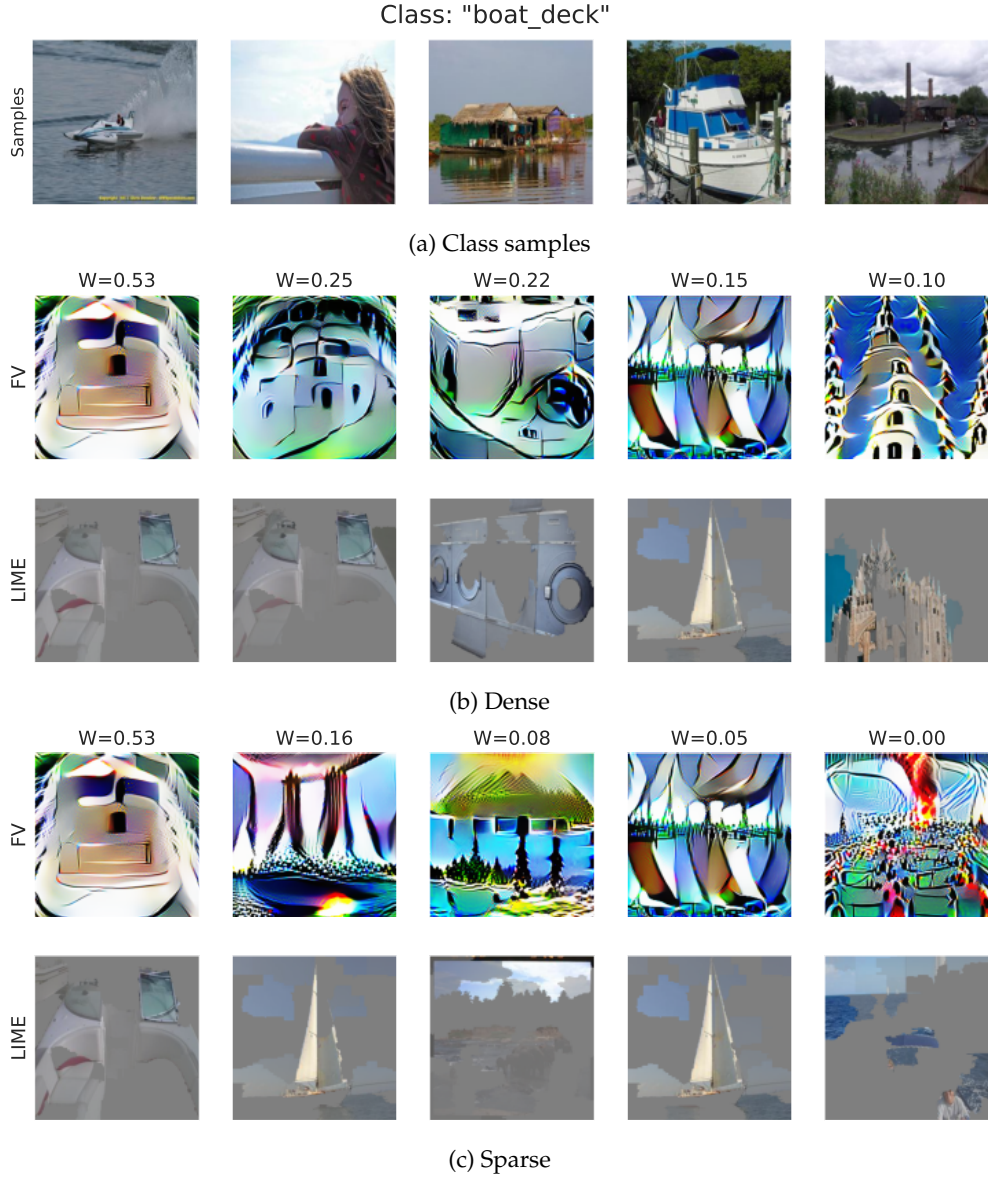


Figure 22: Deep features used by a adversarially-trained ($\epsilon = 3$) ResNet-50 with dense (*middle*) and sparse decision layers (*bottom*) for a randomly-chosen Places-10 class. For each (deep) feature, we show its corresponding linear coefficient in the decision layer (W), along with feature interpretations in the form of feature visualizations (FV) and LIME superpixels.

This HIT is part of an MIT scientific research project conducted by MadryLab. Your decision to complete this HIT is voluntary. There is no way for us to identify you. The only information we will have, in addition to your responses, is the time at which you completed the survey. The results of the research may be presented at scientific meetings or published in scientific journals. Clicking on the 'SUBMIT' button on the bottom of this page indicates that you are at least 18 years of age and agree to complete this HIT voluntarily.

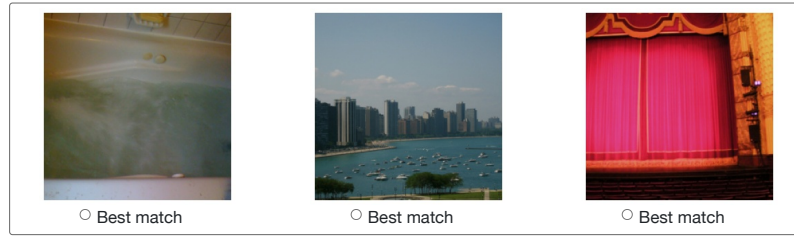
Which image matches the patterns best?

We have trained an AI to recognize objects of one particular type (e.g., "car") in real world images. To detect objects of this type, our AI looks for five patterns (shown below) in a given image. Your task is to (1) inspect the patterns and (2) from a given set of images, choose the one that you think is *most likely to match* the object that the AI is looking for.

Although all five patterns are used by the AI to detect objects of this type, their relative importance might vary. The actual importance of each pattern to the AI (on a scale of 0-100) is displayed below the pattern itself. Note that a **higher** value indicates **greater importance**.



From the images below, choose the one that according to you is most likely to match the object the AI is looking for



How confident are you about your selections?

- ☐ 0 (no confidence)
 ☐ 1 (slightly confident)
 ☐ 2 (moderately confident)
 ☐ 3 (strongly confident)

Figure 23: Sample MTurk task to assess how amenable models with dense/sparse decision layers are to human understanding.

D.4 Human evaluation

We now detail the setup of our MTurk study from Section 3.3. For our analysis, we use a ResNet-50 that has been adversarially-trained ($\epsilon = 3$) on the ImageNet dataset. To obtain a sparse decision layer, we then train a sequence of GLMs via elastic net (cf. Section 2.1) on the deep representation of this network. Based on a validation set, we choose a single sparse decision layer—with 57.65% test accuracy and 39.18 deep features/class on average.

Task setup Recall that our objective is to assess how effectively annotators are able to simulate the predictions of a model when they are exposed to its (dense or sparse) decision layer. To this end, we first randomly select 100 ImageNet classes. Then, for each such ‘target class’ and decision layer (dense/sparse) pair, we created a task by:

1. **Selecting deep features:** We randomly-select *five* deep features utilized by the decision layer to recognize objects of the target class. To make the comparison more fair, we restrict our attention to deep features that are assigned significant weight ($>5\%$ of the maximum) by the corresponding model. We then present these deep features to annotators via feature visualizations. Also shown alongside are

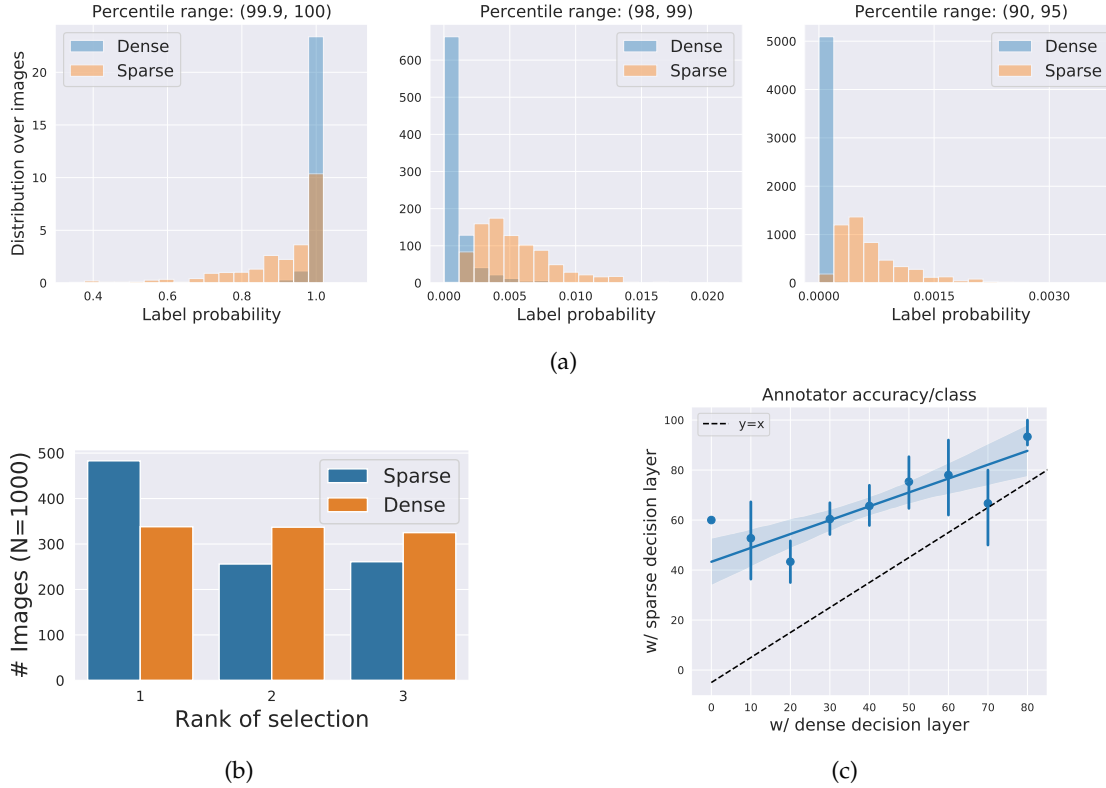


Figure 24: (a) Distribution of the target label probability assigned by the model (with a dense/sparse decision layer) to image candidates used in our MTurk Study. (b) Distribution of images selected by annotators in terms of the ranking of their target class probability. Here, a rank of k implies that the selected image has the k -th highest probability of the target class (out of the 3 images) according to the model. (c) Per-class accuracy of annotators in simulating the predictions of models with dense/sparse decision layer.

the (normalized and rescaled) linear coefficients for each deep feature.

2. **Selecting test inputs:** We rank all the test set ImageNet images based on the probability assigned by the corresponding model (i.e., the ResNet-50 with a dense/sparse decision layer) to the target class. We then randomly select three images, such that they lie in the following percentile ranges in terms of target class probability: (90, 95), (98, 99) and (99.99, 100). Note that since ImageNet has 1000 diverse object categories, the target class probability of a randomly sampled image from the dataset is likely to be extremely small. Thus, fixing the percentiles as described above allows us to pick image candidates that are: (i) somewhat relevant to the target class; and (ii) of comparable difficulty for both types of decision layers. In Figure 24a, we present the target probability distribution as per the model for image candidates selected in this manner.

Finally, annotators are presented with the deep features chosen above—describing them as patterns used by an AI model to recognize objects of a certain (unspecified) type. They are then asked to pick one of the image candidates (randomly-permuted) that best matches the patterns. Annotators are also asked to mark their confidence on a likert scale. A sample task is shown in Figure 23.

For each target label-decision layer pair, we obtain 10 tasks by repeating the random selection process above. This results in a total of 2000 tasks (100 classes \times 2 models \times 10 tasks/(class, model)). Each task is presented to 5 annotators, compensated at \$0.04 per task.

Quality control For each task, we aggregated results over all the annotators. While doing so, we eliminated individual instances where a particular annotator made no selections. We also completely eliminated

instances corresponding to annotators who consistently (>80% of the times) left the tasks blank. Finally, while reporting our results, we only keep tasks for which we have selections from at least two (of five) annotators. We determine the final selection based on a majority vote over annotators, weighted by their confidence.

Results In Table 25, we report annotator accuracy—in terms of their ability to correctly identify the image with the highest target class probability as per the model. We also present a break down of the overall accuracy depending on whether or not the “correct image” is from the target class. We find that sparsity significantly boosts annotators’ ability to intuit (simulate) the model—by nearly 30%. In fact, their performance on models with dense decision layers is close to chance (33%). Note also that for models with sparse decision layers, annotators are able to correctly simulate the predictions *even* when the correct image belongs to a different class.

Accuracy (%)	Dense	Sparse
Overall	35.61 \pm 3.09	63.02 \pm 3.02
From target class	44.02 \pm 5.02	72.22 \pm 4.74
From another class	30.64 \pm 3.65	57.33 \pm 4.00

Table 25: Accuracy of annotators at simulating the model given explanations from the dense and sparse classifiers.

In Figure 24b, we visualize how the image selected by annotators ranks in terms of the model’s target class probability, over all tasks. Note that a rank of one implies that the annotators correctly selected the image which the model predicts as having highest target class probability. This figure largely corroborates the findings in 25—in particular, highlighting that for the standard (dense) decision layer, annotator selections are near-random. In Figure 24c, we visualize annotator accuracy—aggregated per (the 10 tasks for a) target class—for models with dense and sparse decision layers.

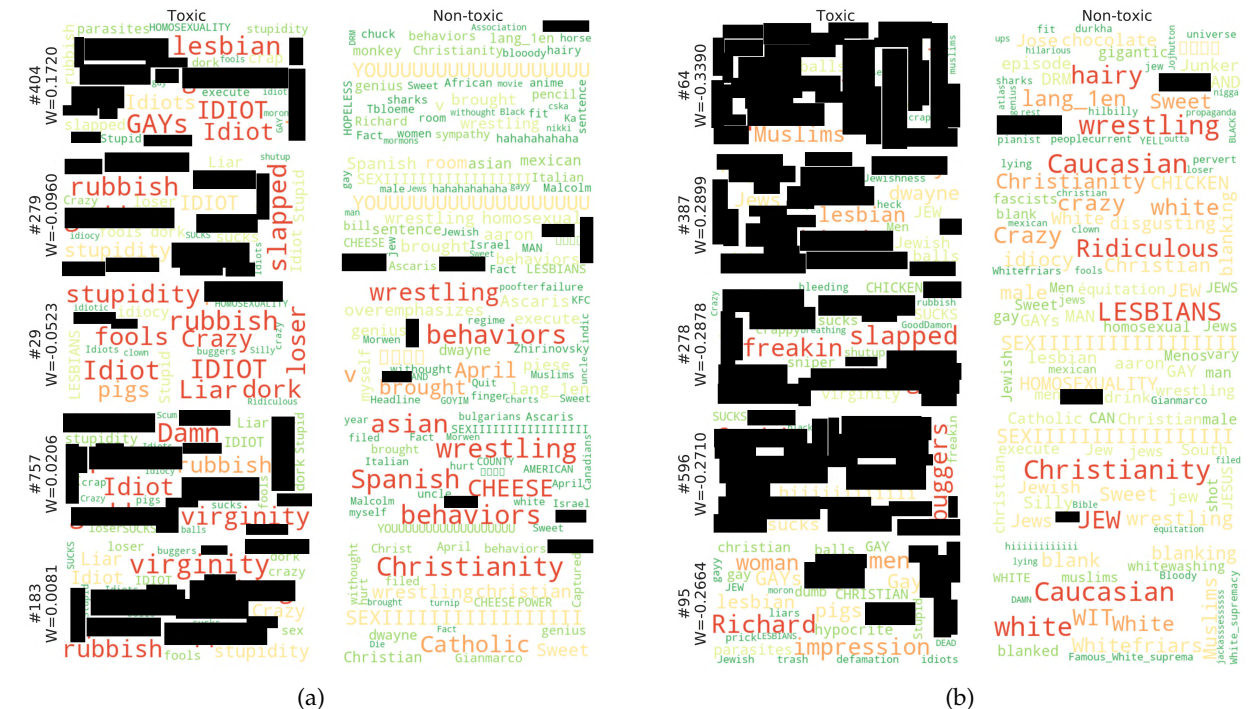
E Model biases and spurious correlations

E.1 Toxic comments

In this section, we visualize the word clouds for the toxic comment classifiers which reveal the biases that the model has learned from the data. Note that these figures are heavily redacted due to the nature of these comments.

In Figure 26, we visualize the top five features for the sparse (Figure 26a) and dense (Figure 26b) decision layers of Toxic-Bert. We note that more of the words in the sparse decision layer refer to identity groups, whereas this is less clear in the dense decision layer. Even if we expand our interpretation to the top 10 neurons with the largest weight, only 7.5% of the words refer to identity groups for the model with a dense decision layer.

In Figure 27, we perform a similar visualization as for the Toxic-BERT model, but for the Debiased-BERT model. The word clouds for the sparse decision layer (Figure 27a) provide evidence that the Debiased-BERT model no longer uses identity words as prevalently for identifying toxic comments. However, it is especially clear from the word clouds for the sparse decision layer that a significant fraction of the non-toxic word clouds contain identity words. This suggests that the model now uses these identity words as strong evidence for non-toxicity, which can be also reflected to a lesser degree in the wordclouds for the dense decision layer (Figure 27b).



E.2 ImageNet

E.2.1 Human study

We now detail the setup of our MTurk study from Section 4.1. For our analysis, we use a standard ResNet-50 trained on the ImageNet dataset—with the default (dense) decision layer, as well as its sparse counterpart from Figure 3b.

Task setup. This task is designed to semi-automatically identify learned correlations in classifiers with dense/sparse decision layers. To this end, we randomly-select 1000 class pairs from each model, such that the classes share a common deep feature in the decision layer. We only consider features to which the model assigns a substantial weight for both classes ($>5\%$ maximum weight). Then, for each class (from the pair), we select the three images that maximally activate the deep feature of interest. Doing so allows us to identify the most prototypical images from each class for the given deep feature.

We then present annotators on MTurk with the six chosen images, grouped by class along with the label. We ask them: (a) whether the images share a common pattern; (b) how confident they are about this selection on a likert scale; (c) to provide a short free text description of the pattern; and (d) for each class, to determine if the pattern is part of the class object or the surrounding. A sample task is shown in Figure 28. Each task was presented to 5 annotators, compensated at \$0.07 per task.

Quality control For each task, we aggregated results over all the annotators. While doing so, we eliminated individual instances where a particular annotator made no selections. We also completely eliminated instances corresponding to annotators who consistently ($>80\%$ of the time) left the task blank. Finally, while reporting our results, we only keep tasks for which we have selections from at least three (of five) annotators. We determine the final selection based on a majority vote over annotators, weighted by their confidence.

E.2.2 Additional visualizations of spurious correlations

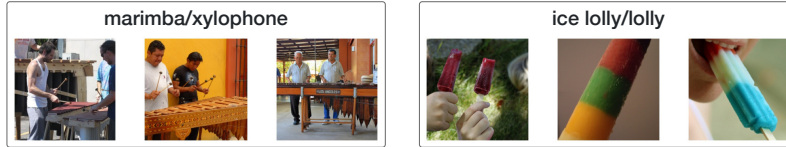
In Figure 29, we provide additional examples of correlations detected using our MTurk study. Then in Figure 30, we summarize annotator-provided descriptions for all the patterns identified in ImageNet classifiers with sparse decision layers via a word cloud. This visualization sheds light into the nature of correlations extracted by ImageNet classifiers from their training data—for instance, we see that the patterns most frequently identified by annotators relate to object color and shape.

This HIT is part of an MIT scientific research project conducted by MadryLab. Your decision to complete this HIT is voluntary. There is no way for us to identify you. The only information we will have, in addition to your responses, is the time at which you completed the survey. The results of the research may be presented at scientific meetings or published in scientific journals. Clicking on the "SUBMIT" button on the bottom of this page indicates that you are at least 18 years of age and agree to complete this HIT voluntarily.

Do you see a common pattern in these images?

You will be shown images belonging to two object categories: "**marimba/xylophone**" and "**ice lolly/lolly**". Your task is to inspect the images, judge whether you can **see a prominent common pattern** between all these images, and then answer the questions below.

Inspect the following images



Question 1: In these six images, do you see a prominent common pattern?

An example of such a pattern could be "red color" or "mountains". If you do not see a distinct common pattern between the images, answer *no*.

☐ Yes ☐ No

Question 2: How confident are you about your selections in Question 1?

☐ 0 (no confidence) ☐ 1 (slightly confident) ☐ 2 (moderately confident) ☐ 3 (strongly confident)

Question 3: Describe the pattern using a word or a short phrase (less than 5 words; skip if your answer to question 1 was *No*.)

An example of such a description could be "red color" or "mountains". Skip if your answer to question 1 was *no*.

A short sentence or a few keywords

Question 4: Is this pattern a part of "**marimba/xylophone**"s or is it present in the surroundings? (Skip if your answer to question 1 was *No*.)

For e.g., the pattern "wheel" is a part of the object "car", whereas the pattern "road" is a part of its surroundings. Similarly, the pattern "leg" is a part of the object "chair", whereas the pattern "pillow" is part of its surroundings.

☐ Part of object ☐ Part of surroundings

Question 5: Is this pattern a part of "**ice lolly/lolly**"s or is it present in the surroundings? (Skip if your answer to question 1 was *No*.)

For e.g., the pattern "wheel" is a part of the object "car", whereas the pattern "road" is a part of its surroundings. Similarly, the pattern "leg" is a part of the object "chair", whereas the pattern "pillow" is part of its surroundings.

Figure 28: Sample MTurk task to diagnose (spurious) correlations in deep networks via their dense/sparse decision layers.

Pattern descriptions
(via MTurk)

Class pairs

all the color.
red in
color object

"hummingbird"



"rose hip"



things. green
cut colour the
color both

"lawn mower"



"zucchini/courgette"



both found in
mountain high

"marmot"



"alp"



orange
color

"butternut squash"



"seashore/coast"



Figure 29: Additional examples of correlations in ImageNet models detected using our MTurk study. Each row contains prototypical images from a pair of classes, along with the annotator-provided descriptions for the shared deep feature that these images strongly activate. For each class, we also display if annotators marked the feature to be a "spurious correlation".

Algorithm 3 Counterfactual generation for a sentence of n words $x = (x_1, \dots, x_n)$, a deep encoder $h : \mathbb{R}^n \rightarrow \mathbb{R}^m$, and a linear decision layer with coefficients (w, b) .

```

1:  $z = h(x)$  // calculate deep features
2:  $y = \arg \max_y w_y z + b_y$  // calculate prediction
3:  $Z^+, Z^- = \emptyset, \emptyset$  // initialize candidate word substitutions
4: for  $i = 1 \dots m$  do
5:   for  $j = 1 \dots n$  do
6:     if  $x_j \in \text{WordCloud}^+(z_i) \wedge w_{yi} > 0$  then
7:        $Z^+ = Z^+ \cup \{(x_j, z_i)\}$  // candidate word substitution with positive weight and positive activation
8:     else if  $x_j \in \text{WordCloud}^-(z_i) \wedge w_{yi} < 0$  then
9:        $Z^- = Z^- \cup \{(x_j, z_i)\}$  // candidate word substitution with negative weight and negative activation
10:    end if
11:  end for
12: end for
13: if  $|Z^+ \cup Z^-| = 0$  then
14:   return -1 // No overlapping words found for counterfactual generation
15: end if
16: Randomly select  $(x_j, z_i) \in Z^+ \cup Z^-$  // select a random word to substitute and its corresponding feature
17: if  $(x_j, z_i) \in Z^+$  then
18:   Randomly select  $\hat{x}_j \in \text{WordCloud}^-(z_i)$  // if positive, select a random negative word
19: else if  $(x_j, z_i) \in Z^-$  then
20:   Randomly select  $\hat{x}_j \in \text{WordCloud}^+(z_i)$  // if negative, select a random positive word
21: end if
22:  $\hat{x} = (x_1, \dots, x_{j-1}, \hat{x}_j, x_{j+1}, \dots, x_n)$  // perform word substitution
23: return  $\hat{x}$  // return generated counterfactual

```

layer (or vice versa). For our sentiment counterfactual experiments, we restrict our analysis to sentences which have counterfactuals in both the sparse and dense decision layers. However, we found that similar results hold if one considers all possible counterfactuals for each individual model instead.

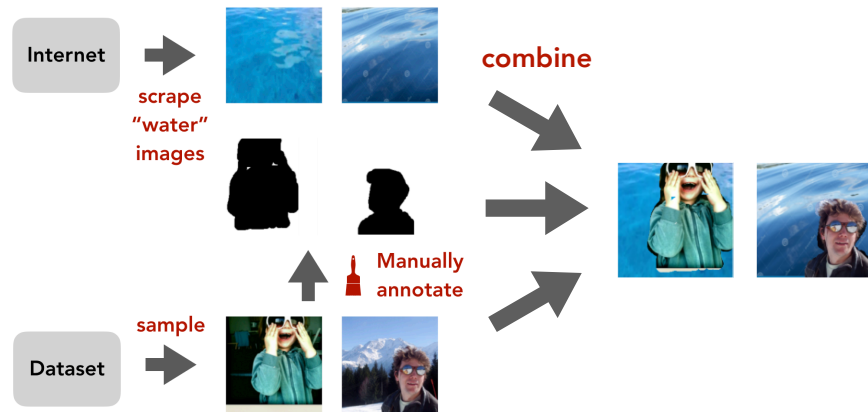


Figure 31: Image counterfactual generation process. We start with a correlation identified during our MTurk study in Section 4.1—for example, the model associates “water” with the class “snorkel”. To generate the counterfactuals shown in Figure 7a, we first select images from other ImageNet classes. We then manually annotate regions in these images to replace with “water” backgrounds obtained via automated image search on the Internet. Finally, we additively combine the “water” backgrounds and the original images, weighted by the mask, to obtain the resulting counterfactual inputs.

F.2 ImageNet counterfactuals

In Figure 31, we illustrate our pipeline for counterfactual image generation. Our starting point is a particular spurious correlation (between a data pattern and a target class) identified via the MTurk study in Section 4.1. We then select images from other ImageNet classes to add the spurious pattern to, and annotate the relevant region where it should be added. We obtain the spurious patterns by automatically scraping search engines. Finally, we combine the original images with the retrieved spurious pattern, using the mask as the weighting, to obtain the desired counterfactual images. These images are then supplied to the model, to test whether the addition of the spurious input pattern indeed fools the model into perceiving the counterfactuals as belonging to the target class.

G Validating ImageNet misclassifications

G.1 Human study

We now detail the setup of our MTurk study from Section 3.3. For our analysis, we use a ResNet-50 that has been adversarially-trained ($\epsilon = 3$) on the ImageNet dataset. To obtain a sparse decision layer, we then train a sequence of GLMs via elastic net (cf. Section 2.1) on the deep representation of this network. Based on a validation set, we choose a single sparse decision layer—with 57.65% test accuracy and 39.18 deep features/class on average.

Task setup. In this task, our goal is to understand if annotators can identify data patterns that are responsible for misclassifications. To this end, we start by identifying deep features that are strongly activated for misclassified inputs.

For any misclassified input x with ground truth label l and predicted class p , we can compute for every deep feature $f_i(x)$:

$$\gamma_i = W[p, i] \cdot f_i(x) - W[l, i] \cdot f_i(x) \quad (8)$$

where W is the weight matrix of the decision layer. Intuitively, this score measures the extent to which a deep feature contributes to the predicted class, relative to its contribution to the ground truth class. Then, sorting deep features based on decreasing/increasing values of this score, gives us a measure of how important each of them are for the predicted/ground truth label. Let us denote f_p as the deep feature with the highest score γ_i and f_l as the one with the lowest.

We find that for the robust ResNet-50 model with a sparse decision layer, the single top deep feature based on this score (f_p) alone is responsible for 26% of the misclassifications (5673 examples in all). That is, for each of these examples, simply turning $f_p = 0$ flips the model’s prediction from p to l . We henceforth refer to these deep features (one per misclassified input) as “problematic” features.

For our task, we randomly subsample 1330 of the aforementioned 5673 misclassified inputs. We then construct MTurk tasks, wherein annotators are presented with one such input (without any information about the ground truth or predicted labels), along with the feature visualizations for two deep features. These two features are either (with equal probability):

- (f_l, f_p) : The deep features which (relatively) contribute most to the ground truth and predicted class respectively.
- (f_l, f_r) : The deep feature which (relatively) contributes most to the ground truth class, along with a randomly-chosen one (out of the 2048 possible deep features). This is meant to serve as a control.

Annotators are then asked: (a) to select all the patterns (i.e., feature visualization of a deep feature) that match the image; (b) to select the one that best matches the image (if they selected both in (a)); (c) to mark their confidence on a likert scale. A sample task is shown in Figure 32. Each task was presented to 5 annotators, compensated at \$0.03 per task.

Note that, in the case where the ground truth label for each image is actually pertinent to it and that model relies on semantically-meaningful deep features for every class, we would expect annotators to select f_l to match the image 100% of the time. On the other hand, we would expect that annotators rarely select f_r to match the image.

This HIT is part of an MIT scientific research project conducted by MadryLab. Your decision to complete this HIT is voluntary. There is no way for us to identify you. The only information we will have, in addition to your responses, is the time at which you completed the survey. The results of the research may be presented at scientific meetings or published in scientific journals. Clicking on the 'SUBMIT' button on the bottom of this page indicates that you are at least 18 years of age and agree to complete this HIT voluntarily.

Identify the patterns that match the given image

Please inspect the image and patterns below, and answer the following questions.

Task 1: Select all the patterns that match the image shown on the left.

Please select at least one pattern. Select both patterns only in cases where you strongly believe that they are both visually similar to the image.



☐ Matches image



☐ Matches image



Task 2: Which of the two patterns matches the given image *better* according to you?
(Answer only if you selected both patterns in Task 1)



☐ Best match



☐ Best match

Task 3: How confident are you about your selections?

- ☐ 0 (no confidence)
 ☐ 1 (slightly confident)
 ☐ 2 (moderately confident)
 ☐ 3 (strongly confident)

Figure 32: Sample MTurk task to identify input patterns responsible for the misclassifications in deep networks with the help of their (sparse) decision layers.

Quality control For each task, we aggregated results over all the annotators. While doing so, we eliminated individual instances where a particular annotator made no selections. We also completely eliminated

instances corresponding to annotators who consistently ($>80\%$ of the times) left the task blank. Finally, while reporting our results, we only keep tasks for which we have selections from at least two (of five) annotators. We determine the final selection based on a majority vote over annotators, weighted by their confidence.

G.2 Additional error visualizations

In Figure 33, we present additional examples of misclassifications for which annotators the top deep feature used by the sparse decision layer to detect the predicted class to be a better match for the image than the corresponding top feature for the ground truth class.



Figure 33: Additional examples of misclassified ImageNet images for which annotators deem the top activated feature for the predicted class (*rightmost*) as a better match than the top activated feature for the ground truth class (*middle*).

G.3 Model confusion

In Figure 34, we visualize the correlation between model confusion within a pair of classes, and the number of shared features between them in the sparse decision layer. Model confusion within a class pair (i, j) is measured as $\max(C_{(i,j)}, C_{(j,i)})$, where C is the overall confusion matrix. We find that for models with sparse decision layers, the feature overlap between two classes, is significantly correlated with model errors within that class pair. One can thus inspect the corresponding shared features—cf. Figure 35 for an example—to better understand the underlying causes for inter-class model confusion.

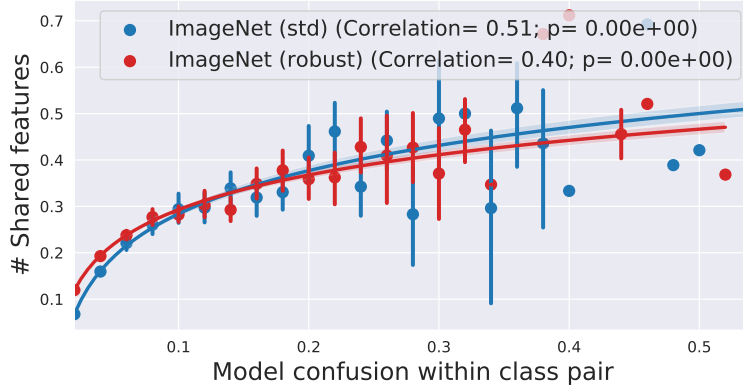


Figure 34: Correlation between the number of features shared in the sparse decision layer of a model for two classes, and model confusion between them. Model confusion within a class pair is measured as the maximum of the corresponding entries $(C_{(i,j)}, C_{(j,i)})$ of the overall confusion matrix.

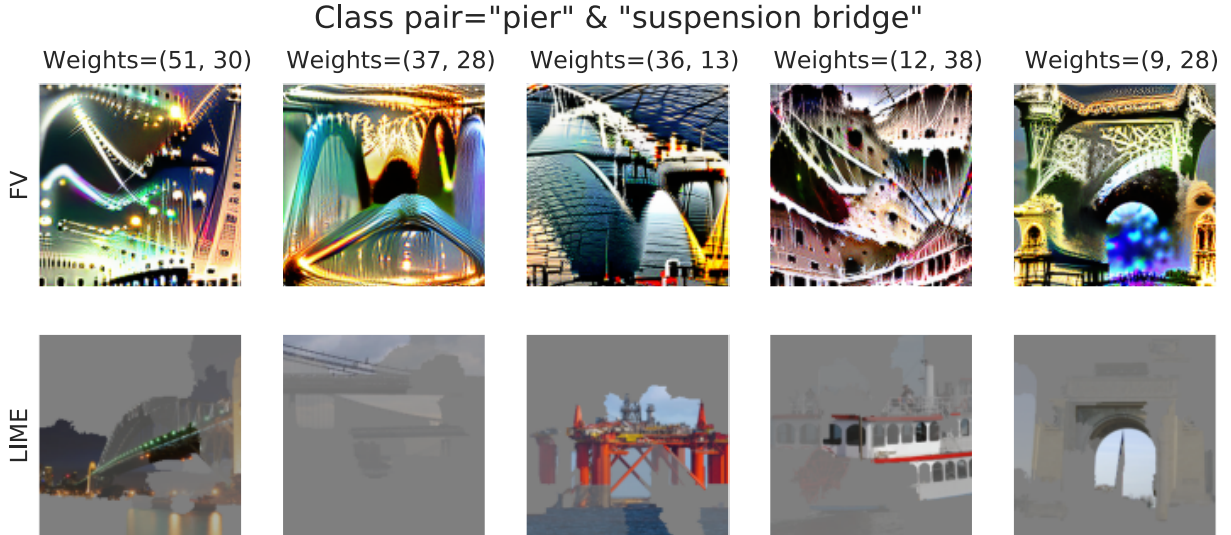


Figure 35: Sample visualization of confusing features: Five of the deep features used by a robust ($\epsilon = 3$) ImageNet-trained ResNet-50 with sparse decision layer to identify objects of classes “pier” and “suspension bridge” which are frequently confused by the model ($C_{i,j}$ and $C_{j,i}$ are 16% and 24% respectively). Each of these deep features is interpreted using feature visualizations (FV) and LIME superpixels; shown alongside their linear coefficients (W).